



Terrestrial Ecosystem Model in R (TEMIR) version 1.0: Simulating ecophysiological responses of vegetation to atmospheric chemical and meteorological changes

Amos P. K. Tai^{1,2,3}, David H. Y. Yung¹, and Timothy Lam^{2,4}

5 ¹ Earth and Environmental Sciences Programme and Graduate Division of Earth and Atmospheric Sciences, Faculty of Science, The Chinese University of Hong Kong, Hong Kong, China

² Institute of Environment, Energy and Sustainability, The Chinese University of Hong Kong, Hong Kong, China

³ State Key Laboratory of Agrobiotechnology, The Chinese University of Hong Kong, Hong Kong, China

⁴ Centre for Doctoral Training in Environmental Intelligence, University of Exeter, Exeter, UK

10 *Correspondence to:* Amos P. K. Tai (amostai@cuhk.edu.hk)

Abstract. The newly developed offline land ecosystem model Terrestrial Ecosystem Model in R (TEMIR) version 1.0 is described here. This version of the model simulates plant ecophysiological (e.g., photosynthetic, stomatal) responses to varying meteorological conditions and concentrations of CO₂ and ground-level ozone (O₃) based on prescribed meteorological and atmospheric chemical inputs from various sources. Driven by the same meteorological data used in the GEOS-Chem chemical transport model, this allows asynchronously coupled experiments with GEOS-Chem simulations with unique coherency for investigating biosphere-atmosphere chemical interactions. TEMIR agrees well with FLUXNET site-level gross primary productivity (GPP) in terms of both the diurnal and monthly cycles (correlation coefficients $R^2 > 0.85$ and $R^2 > 0.8$, respectively) for most plant functional types (PFTs). Grass and shrub PFTs have larger biases due to generic model representations. The model performs best when driven by local site-level meteorology rather than reanalyzed gridded meteorology. Simulation using gridded meteorology agrees well for annual GPP in seasonality and spatial distribution with a global average of 134 Pg C yr⁻¹. Application of Monin-Obukhov similarity theory to infer canopy conditions from gridded meteorology does not improve model performance, predicting a uniform increase of +21% for global GPP. Present-day O₃ concentrations simulated by GEOS-Chem and an O₃ damage scheme at high sensitivity show a 2% reduction in global GPP with prominent reductions by up to 15% in eastern China and the eastern US. Regional correlations are generally unchanged when O₃ is present, and biases are reduced especially for regions with high O₃ damages. An increase in atmospheric CO₂ concentration by 20 ppmv from year-2000 to year-2010 level modestly decreases O₃ damage due to reduced stomatal uptake, consistent with ecophysiological understanding. Our work showcases the utility of this version of TEMIR for evaluating biogeophysical responses of vegetation to changes in atmospheric composition and meteorological conditions.



1 Introduction

Terrestrial vegetation, as an integral part of the global biosphere, plays many vital roles regulating the Earth system. It facilitates a substantial portion of the global land-atmosphere exchange of energy, momentum and chemical species relevant for climate and atmospheric chemistry. It is a major sink for atmospheric carbon, sequestering an estimated 123 ± 8 Pg C of carbon dioxide (CO₂) from the atmosphere annually through plant photosynthesis (Le Quéré et al., 2015; Beer et al., 2010), albeit with a relatively large observation-constrained range of 119–175 Pg C yr⁻¹. This vegetation-mediated process of CO₂ sequestration, also known as gross primary productivity (GPP), is a key regulator of climate, and forests in particular are one of the largest providers of climate services (Bonan, 2008). Even before the industrial revolution, human perturbations of natural vegetation for agriculture, timber and other uses have had significant impacts on the natural carbon cycle. About a third of the total cumulative CO₂ emission to date due to anthropogenic land cover change could have been emitted before the time of industrialization (Pongratz et al. 2009). Over the 20th century, widespread deforestation was estimated to result in a net warming of 0.13–0.15°C due to biogeochemical warming (via carbon emission) partly offset by biogeophysical cooling (via higher albedo) (Pongratz et al., 2010). A reversal of historical land use trends, especially in the form of afforestation and careful management and preservation of existing forests, has the potential to help mitigate anthropogenic climate change, but the future carbon uptake capacity of forests can be substantially altered by an array of biogeochemical feedback mechanisms as forest ecosystems respond to changing climate and atmospheric composition (Arneeth et al., 2010). Various global terrestrial ecosystem models have been employed, either standalone or coupled within an earth system model, to estimate future carbon budgets in response to global change; a multi-model comparison estimated that over the 21st century, the terrestrial biosphere can gain 0.2–1.5 Pg C for 1 part per million by volume (ppmv) increase in CO₂ due to fertilization effect, but lose 10–90 Pg C per degree increase in global surface temperature as forest ecosystems experience warming and more climatic stress (Arora et al., 2013).

An emerging research interest is the interactions between the terrestrial biosphere and atmospheric chemistry, and the roles of short-lived atmospheric species in modulating terrestrial ecosystem functions. On the one hand, terrestrial ecosystems facilitate the removal of air pollutants from the atmosphere via the process of dry deposition, thus providing another important service for human benefits. The consequent health benefits are substantial: 17.4 million tons of air pollutants equivalent to US\$6.8 billion of public health cost was removed by forests in the contiguous US in 2010 alone (Nowak et al., 2014), which is 6% of estimated total health cost of US\$109 (EUR145 billion) due to air pollution in the US of 2010 (Im et al., 2018). Globally it is estimated that dry deposition onto vegetated surfaces accounts for ~20% of the loss of tropospheric O₃ (Wild, 2007), which is a major air pollutant detrimental to human health. On the other hand, the depositional uptake of O₃ by leaves incurs substantial damage to vegetation, interfering with ecosystem functions and terrestrial biogeochemical cycling. In the process of dry deposition, O₃ diffuses via leaf openings known as stomata into the leaf interior, where it impairs plant physiological functions and health; stomatal uptake itself is responsible for 30–90% of the deposition sink of O₃ (Felzer et al., 2007; Ainsworth et al.,



2012). O₃ can significantly disrupt leaf photosynthesis rates, thereby hindering plant growth and reducing forest and crop productivity (Ainsworth et al., 2012). The O₃-induced global yield losses for the key staple crops (wheat, rice, maize and soybean) for year 2000 were estimated to be worth US\$11–26 billion (Van Dingenen et al., 2009; Avnery et al., 2011a). For natural vegetation and forests, observed GPP reductions average at ~10% but could regionally be up to 30% (e.g., Fares et al., 5 2013; Proietti et al., 2016; Moura et al., 2018). Modeling studies have estimated a 2–12% decrease in GPP due to present-day O₃, with large reductions of more than 20% in the midlatitude regions of North America, Europe and East Asia (Lombardozzi et al., 2015; Yue and Unger, 2014; Anav et al., 2011). O₃ damage to plants in turn alters biosphere-atmosphere exchange, with ramifications for both climate and air quality. Models have estimated a 2–6% decrease in global transpiration following O₃ damage. The corresponding reductions in latent heat flux can regionally enhance temperature by up to 2–3°C and alter rainfall 10 (Li et al., 2016; Sadiq et al., 2017; Zhu et al., 2022).

Accurate predictions of both air quality and ecosystem functions, as well as their interactions, thus require proper representation of ecophysiological processes in the terrestrial ecosystems, but are obscured by a complex array of nonlinear interactions between plant physiology, O₃, CO₂ and meteorological drivers. Elevated CO₂ enhances photosynthesis and also induces 15 stomatal closure (reducing stomatal conductance) over various timescales, likely reflecting the adaptation of plants to improve water use efficiency (e.g., Noormets et al., 2010; Franks et al., 2013). Sanderson et al. (2007) suggested that a doubling of CO₂ could worsen O₃ air quality by up to +8 ppbv (parts per billion by volume) due to reduced stomatal conductance and dry deposition. O₃ damage on vegetation can potentially lead to a decline in leaf area index (LAI) and stomatal uptake, which in turn creates a strong positive feedback that further enhances surface O₃ by up to +6 ppbv (Sadiq et al., 2017; Zhou et al., 2018; 20 Zhu et al., 2022). Furthermore, a higher humidity generally promotes stomatal opening, while drought conditions often inhibit it (Dermody et al., 2008; Rhea et al., 2010; Monks et al., 2015). A modeling study by Emberson et al. (2013) suggested that the extended drought in association with the 2006 European heat wave might have shut down the dry-depositional sink for O₃ as plants closed their stomata to prevent excessive water loss, thereby leading to a greater number of O₃-related premature human deaths. To complicate the matter further, O₃ damage may cause stomata to respond more sluggishly to meteorological 25 conditions; under certain prolonged conditions (e.g., droughts) such a sluggishness of stomatal response may cause them to be more open than without O₃ damage (McLaughlin et al., 2007; Sun et al., 2012; Huntingford et al., 2018). These studies highlight the importance of considering the adaptive responses of plants to changing atmospheric composition and meteorological conditions in predicting future O₃ air quality and ecosystem productivity. Yet, most atmospheric chemistry models to date rely on semi-empirical formulations for plant-mediated processes (e.g., dry deposition) without resolving 30 ecophysiological processes that may evolve over time; issues may also arise when coupling atmospheric chemistry and complex ecosystem models due to inconsistent driving inputs and model requirements (Clifton et al., 2020). As interpretation of model results depends largely on the underlying physiological processes, in-depth understanding of system behaviors is crucial yet lacking (Ganzeveld and Lelieveld, 1995; Hardacre et al., 2015).



A number of studies have taken advantage of the Earth system modeling framework (ESMF) to dynamically link dry deposition and O₃ fluxes in the atmospheric chemistry model to the photosynthetic and stomatal calculations in the land surface model (e.g., Ganzeveld et al., 2010; Pacifico et al., 2012; Val Martin et al., 2014; Verbeke et al., 2015; Halladay and Good, 2017; Sadiq et al., 2017; Zhu et al., 2022). These studies largely focused on long-term averages and trends rather than variability due to climate anomalies. Simulated climate is also often sensitive to land surface changes, and any simulated responses of meteorological variables to plant ecophysiological changes can further modify O₃ through a cascade of feedbacks, potentially obscuring the importance and relative contribution from individual plant-mediated pathways. Fully coupled Earth system models contain intricate network of interdependencies among climate, atmospheric chemistry and the land surface, thus may not be ideal for calibrating specific model processes against observations. Standalone or coupled chemical transport models and ecosystem models driven by a consistent set of prescribed “offline” meteorology from observations and reanalysis datasets would be particularly useful to improve the understanding of O₃-vegetation interactions in isolation and enhance model capability in predicting air quality under climate anomalies.

The Terrestrial Ecosystem Model in R version 1.0 (TEMIR v1.0), described in Sect. 2.2, is a standalone, multi-parameterization model designed to simulate important canopy and ecophysiological processes that are relevant for ecosystem exchange and atmospheric chemistry, including canopy radiative physics and aerodynamics, photosynthesis, stomatal behaviors, and dry deposition of different chemical species. It is designed to be entirely consistent with the GEOS-Chem global chemical transport model (CTM) in terms of model inputs and land surface representation. Driven by a consistent set of prescribed meteorological and surface flux inputs, asynchronously coupled GEOS-Chem-TEMIR experiments can be performed globally or regionally to simulate plant ecophysiological responses to changing atmospheric composition arising from, e.g., O₃ pollution and rising CO₂, as well as to a changing climate as simulated by climate models that have already been coupled to GEOS-Chem. It can also be used with user-defined meteorological and flux inputs (especially those directly from FLUXNET observations; <https://fluxnet.fluxdata.org>) to perform site-level simulations for various purposes, e.g., process investigation, predictions, model validation and optimization with different parameterization schemes. Versions of TEMIR with active biogeochemistry and crop biophysics are under development and not within the scope of this paper. Validation and application of TEMIR to simulate O₃ dry deposition and flux-based metrics of O₃ damage on crops have been presented in several previous studies (i.e., Wong et al., 2019; Tai et al., 2021; Sun et al., 2022).

Developing an ecosystem model in the R programming language is beneficial to various ends. R is now a popular tool for ecological research (R Core Team, 2022), especially in population and community ecology; Lai et al. (2019) surveyed more than 60,000 peer-reviewed ecology journal articles, and found that the number of studies reported using R as their primary tool in data analysis increased from ~10% in 2008 to ~60% in 2017. Ecosystem modeling studies, however, historically have closer ties with geoscientific research due to the importance of representing the land cover and biogeochemical cycles in climate models, often making use of more low-level languages typical in Earth system modeling such as Fortran. Having a terrestrial



ecosystem model in R may help enhance the accessibility to ecosystem modeling for ecological researchers, generate a common modeling framework across population, community and ecosystem scales, and hopefully serve as a bridge between ecological and geoscientific fields to advance interdisciplinarity. Being an entirely free and open software as well as a highly versatile and relatively user-friendly programming language, it may also help promote open science in ecosystem research and education, allowing the model to be more widely used as a policy-relevant assessment tool for practitioners.

2 Model description

2.1 GEOS-Chem model description

GEOS-Chem as a global CTM is widely used in research due to its versatility in tackling a multitude of atmospheric chemistry problems. We use GEOS-Chem v12.2.0 (DOI: 10.5281/zenodo.2572887) driven by assimilated meteorological observations from the Goddard Earth Observing System (GEOS) of the NASA Global Modeling Assimilation Office (GMAO) (<http://acmg.seas.harvard.edu/geos/>). The driving meteorological data are available in 1-hourly and 3-hourly temporal resolutions with the finest horizontal resolution of 0.25° latitude by 0.3125° longitude and 72 hybrid vertical levels extending from the surface to 0.01 hPa, provided by the GEOS-Forward Processing product (GEOS-FP). Coarser resolutions of the reanalysis product Modern-Era Retrospective analysis for Research and Applications, Version 2 (MERRA-2) (Gelaro et al., 2017) can also be used, which is a historical dataset spanning from 1980 to the present day. GEOS-Chem is equipped with detailed O₃-NO_x-VOC (volatile organic compounds)-aerosol chemical mechanisms that is used for simulating atmospheric chemistry, and validated in many studies (e.g., Bey et al., 2001; Parrington et al., 2008; Zhang et al., 2010; Zhang and Wang, 2016; Hu et al., 2018). Anthropogenic emissions of many species (e.g., CO, NO_x and non-methane VOCs) can be taken from global inventories (i.e., Community Emissions Data System, CEDS; Hoesly et al., 2018) and/or regional inventories, through the Harmonized Emissions Component (HEMCO) v2.1 (Keller et al., 2014; Lin et al., 2021). Biogenic emissions are calculated online with the Model of Emissions of Gases and Aerosols from Nature (MEGAN) version 2.1 (Guenther et al., 2012). An alternative photosynthesis-based isoprene emission (Pacifico et al., 2011) is also available (Lam et al., 2023). In this study, the meteorological inputs used for global simulations of both GEOS-Chem and TEMIR are the MERRA-2 product at a resolution of 2°×2.5° latitude by longitude. The surface O₃ concentrations simulated by GEOS-Chem are used as inputs for TEMIR to simulate the corresponding vegetation responses under the consistent set of MERRA-2 meteorology.

2.2 TEMIR model description

TEMIR computes biogeophysical responses of terrestrial ecosystems to changes in the atmospheric and terrestrial environment. Driven by consistent meteorological and land surface inputs data as GEOS-Chem, TEMIR is designed to be highly compatible with GEOS-Chem and can be coupled asynchronously with simulated atmospheric composition from GEOS-Chem, which is a vital aspect that allows the biosphere-atmosphere coupling needed for the objectives of this study.



2.2.1 Plant type representation

Plant type categories considered in TEMIR follows the convention of the Community Land Model version 4.5 (CLM4.5) (Oleson and Lawrence, 2013), embedded within the Community Earth System Model (CESM) version 1.2.2 (<http://www.cesm.ucar.edu/models/clm/>). The plant type categories consist of unvegetated or bare ground and a total of 24 different plant function types (PFTs) including 14 natural vegetation types and 10 rainfed or irrigated crop types (Table S1), each with a prescribed present-day fractional coverage or distribution per model grid cell as derived from MODerate resolution Imaging Spectroradiometer (MODIS) satellite data (Lawrence and Chase, 2007), and their own characteristic structural and physiological parameters. The parameters used to represent vegetation structure include leaf area index (LAI), stem area index (SAI) and canopy height (h). Monthly PFT-level LAI is derived from MODIS using the deaggregation methods described in Lawrence and Chase (2007); PFT-level SAI is derived from LAI with the methods of Zeng et al. (2002). PFT-level canopy heights are prescribed following Bonan et al. (2002). PFT distributional and structural data are regridded to the default resolution of MERRA-2 data for TEMIR simulations. Users can specify any grid-level (total) LAI input data; the PFT-level data would be scaled accordingly.

2.2.2 Canopy radiative transfer

Each PFT simulated per vegetated grid cell is represented as a single “big-leaf” canopy of sunlit and shaded leaves. We implement two alternative canopy radiative transfer schemes to calculate the sunlit and shaded LAI (LAI_{sun} , LAI_{sha}), absorbed photosynthetically active radiation (PAR) by sunlit and shaded leaves (ϕ_{sun} , ϕ_{sha} , $W m^{-2}$), canopy light extinction coefficient (K_b), surface albedo and other radiative variables as functions of direct beam and diffuse incident PAR reaching the canopy top (I_{dir} , I_{diff} , $W m^{-2}$), cosine of solar zenith angle (μ) and other vegetation parameters. The default scheme follows the two-stream approximation of Dickinson (1983) and Sellers (1985) which considers light attenuation by both leaves and stems. The details of the scheme is described in Sect. 3.1, 3.3 and 4.1 of Oleson et al. (2013). In brief, the absorbed PAR averaged over the sunlit and shaded canopy per unit plant area (leaf plus stem area) is

$$\phi_{sun} = \frac{f_{sun,dir}I_{dir} + f_{sun,diff}I_{diff}}{PAI_{sun}} \quad (1)$$

$$\phi_{sha} = \frac{f_{sha,dir}I_{dir} + f_{sha,diff}I_{diff}}{PAI_{sha}} \quad (2)$$

where $f_{sun/sha,dir/diff}$ is the fraction of direct/diffuse incident radiation absorbed by the sunlit/shaded leaves and stems as calculated by the two-stream approach; the sunlit and shaded plant area index ($PAI = LAI + SAI$) is

$$PAI_{sun} = \frac{1 - e^{-K_b(LAI+SAI)}}{K_b} \quad (3)$$

$$PAI_{sha} = (LAI + SAI) - PAI_{sun} \quad (4)$$

and K_b is calculated following the two-stream approximation. The sunlit and shaded LAI ultimately used to calculate canopy photosynthesis are

$$LAI_{sun} = PAI_{sun} \frac{LAI}{LAI+SAI} \quad (5)$$



$$LAI_{\text{sha}} = PAI_{\text{sha}} \frac{LAI}{LAI + SAI} \quad (6)$$

An alternative, simplified scheme that accounts for light attenuation by leaves only following the convention of the Zhang et al. (2002) dry deposition model as modified from Norman (1982), which is also implemented in TEMIR (see Sect. 2.2.6), is implemented as follows:

$$\phi_{\text{sha}} = I_{\text{diff}} \exp(-0.5LAI^a) + 0.07I_{\text{dir}}(1.1 - 0.1LAI) \exp(-\mu) \quad (7)$$

$$\phi_{\text{sun}} = \phi_{\text{sha}} + K_b J_{\text{dir}}^b \quad (8)$$

$$K_b = \frac{0.5}{\mu} \quad (9)$$

$$LAI_{\text{sun}} = \frac{1 - e^{-K_b LAI}}{K_b} \quad (10)$$

$$LAI_{\text{sha}} = LAI - LAI_{\text{sun}} \quad (11)$$

where exponents $a = 0.7$ and $b = 1$ for $LAI < 2.5$ or downwelling shortwave radiation flux $S_{\downarrow} < 200 \text{ W m}^{-2}$, and $a = 0.8$ and $b = 0.8$ otherwise.

2.2.3 Canopy photosynthesis and conductance

Leaf photosynthesis of both C3 and C4 plants is represented by the well-established formulation that relates to Michaelis–Menten enzyme kinetics and photosynthetic biochemical pathways (Farquhar et al., 1980; von Caemmerer and Farquhar, 1981; Collatz et al., 1991, 1992), which considers three limiting regimes:

(i) The Rubisco-limited photosynthesis rate (A_c , $\mu\text{mol CO}_2 \text{ m}^{-2} \text{ s}^{-1}$) captures the rate of carbon assimilation when substrate availability or enzyme activity is the limiting factor:

$$A_c = \begin{cases} V_{\text{cmax}} \frac{c_i - \Gamma_*}{c_i + K_c \left(1 + \frac{o_i}{K_o}\right)} & \text{for C3 plants} \\ V_{\text{cmax}} & \text{for C4 plants} \end{cases} \quad (12)$$

where c_i (Pa) the intercellular CO_2 partial pressure; K_c and K_o are the Michaelis–Menten constants for carboxylation and oxygenation (Pa), respectively; o_i (Pa) is the intercellular oxygen partial pressure; Γ_* (Pa) is the CO_2 compensation point and V_{cmax} ($\mu\text{mol CO}_2 \text{ m}^{-2} \text{ s}^{-1}$) is the maximum rate of carboxylation.

(ii) The RuBP-limited photosynthetic rate (A_j , $\mu\text{mol CO}_2 \text{ m}^{-2} \text{ s}^{-1}$) defines the photosynthesis rate as light intensity and thus RuBP regeneration are the limiting factor:

$$A_j = \begin{cases} \frac{J}{4} \left(\frac{c_i - \Gamma_*}{c_i + 2\Gamma_*} \right) & \text{for C3 plants} \\ 0.23\phi & \text{for C4 plants} \end{cases} \quad (13)$$

where J ($\mu\text{mol m}^{-2} \text{ s}^{-1}$) is the electron transport rate, and ϕ (W m^{-2}) is the absorbed PAR for either sunlit (ϕ_{sun}) or shaded (ϕ_{sha}) leaves as calculated by the canopy radiative transfer model (Sect. 2.2.2). For C3 plants, J is determined by ϕ as well, and is determined as the smaller of the two roots of the quadratic equation:



$$\Theta_{\text{PSII}} J^2 - (I_{\text{PSII}} + J_{\text{max}}) J + I_{\text{PSII}} J_{\text{max}} \quad (14)$$

where J_{max} ($\mu\text{mol m}^{-2} \text{s}^{-1}$) is the maximum potential rate of electron transport; $\Theta = 0.7$ is the curvature parameter; I_{PSII} ($\mu\text{mol m}^{-2} \text{s}^{-1}$) is the light utilized in electron transport by photosystem II, determined by:

$$I_{\text{PSII}} = 2.3 \Phi_{\text{PSII}} \phi \quad (15)$$

5 where $\Phi_{\text{PSII}} = 0.85$ is the quantum yield of photosystem II.

(iii) The product-limited photosynthetic rate (A_p , $\mu\text{mol CO}_2 \text{m}^{-2} \text{s}^{-1}$) represents the limitation from the regeneration rate of photosynthetic phosphate compounds:

$$A_p = \begin{cases} 3 T_p & \text{for C3 plants} \\ k_p \frac{c_i}{P_{\text{atm}}} & \text{for C4 plants} \end{cases} \quad (16)$$

10 where T_p is the triose phosphate utilization rate ($\mu\text{mol m}^{-2} \text{s}^{-1}$), P_{atm} (Pa) is the ambient atmospheric pressure, and k_p is the initial slope of CO_2 response curve for C4 plants. The model considers colimitation as described by (Collatz et al., 1991, 1992), and the leaf-level gross photosynthesis rate (A , $\mu\text{mol CO}_2 \text{m}^{-2} \text{s}^{-1}$) is given by the smaller root of the equations:

$$\Theta_{\text{cj}} A_i^2 - (A_c + A_j) A_i + A_c A_j = 0 \quad (17)$$

$$\Theta_{\text{ip}} A^2 - (A_i + A_p) A + A_i A_p = 0$$

The net photosynthesis rate (A_n , $\mu\text{mol CO}_2 \text{m}^{-2} \text{s}^{-1}$) is then:

$$15 \quad A_n = A - R_d \quad (18)$$

where R_d ($\mu\text{mol CO}_2 \text{m}^{-2} \text{s}^{-1}$) is the dark respiration rate. All of the parameters (V_{cmax} , J_{max} , T_p , R_d , K_c , K_o , Γ^* , k_p) are temperature-dependent and scale with their respective PFT-specific standard values at 25°C by different formulations. Temperature acclimation of V_{cmax} and J_{max} from the previous 10 days as well as daylength dependence of V_{cmax} is implemented as default options. These are all detailed in Sect. 8.2 and 8.3 of Oleson et al. (2013).

20

The calculation of photosynthesis rates described above is coupled with that of stomatal conductance of water (g_s , m s^{-1}) following the formulation of Ball et al. (1987) with m and b being the slope and intercept parameters derived from empirical data:

$$g_s = \alpha \left(m A_n \frac{\frac{e_s}{e_{\text{sat}}}}{P_{\text{atm}}} + b \right) \quad (19)$$

25 where g_s is controlled by the leaf surface CO_2 partial pressure c_s (Pa), leaf surface water vapor pressure e_s (Pa) and temperature-dependent saturation vapor pressure e_{sat} (Pa); $m = 9$ and $b = 10000 \mu\text{mol m}^{-2} \text{s}^{-1}$ for C_3 plants, and $m = 4$ and $b = 40000 \mu\text{mol m}^{-2} \text{s}^{-1}$ for C_3 plants; the factor α converts the unit of conductances from $\mu\text{mol H}_2\text{O m}^{-2} \text{s}^{-1}$, which is more common in ecophysiology literature, to m s^{-1} , which is common in atmospheric science literature:

$$\alpha = \frac{10^{-6} R_{\text{uni}} \theta_{\text{atm}}}{P_{\text{atm}}} \quad (20)$$

30 where $R_{\text{uni}} = 8.314468 \text{ J K}^{-1} \text{ mol}^{-1}$ is the universal gas constant, and θ_{atm} (K) is the ambient atmospheric potential temperature. An alternative stomatal conductance scheme (Medlyn et al., 2011; Franks et al., 2017) is also implemented:



$$g_s = \alpha \left[1.6 \left(1 + \frac{m}{\sqrt{\text{VPD}}} \right) \frac{A_n}{c_s} + b \right] \quad (21)$$

where $\text{VPD} = 0.001(e_{\text{sat}} - e_s)$ (kPa) is the vapor pressure deficit, m has PFT-specific values consistent with CLM5.0 (Sect. 9.3 of Lawrence et al., 2020), and $b = 100 \mu\text{mol m}^{-2} \text{s}^{-1}$. Photosynthesis and stomatal conductance are further related by the diffusive flux equations for CO_2 and water vapor:

$$5 \quad A_n = \frac{1}{\alpha} \left(\frac{1.4}{g_b} + \frac{1.6}{g_s} \right)^{-1} \frac{c_a - c_i}{P_{\text{atm}}} = \frac{g_b}{1.4\alpha} \frac{c_a - c_s}{P_{\text{atm}}} = \frac{g_s}{1.6\alpha} \frac{c_s - c_i}{P_{\text{atm}}} \quad (22)$$

$$E' = \frac{1}{\alpha} \left(\frac{1}{g_b} + \frac{1}{g_s} \right)^{-1} \frac{e_a - e_i}{P_{\text{atm}}} = \frac{g_b}{\alpha} \frac{e_a - e_s}{P_{\text{atm}}} = \frac{g_s}{\alpha} \frac{e_s - e_i}{P_{\text{atm}}} \quad (23)$$

where c_a (Pa) and e_a (Pa) are the canopy air CO_2 partial and water vapor pressure, e_i (Pa) is the saturation vapor pressure at the leaf temperature, E' ($\mu\text{mol H}_2\text{O m}^{-2} \text{s}^{-1}$) is the transpiration flux, and g_b (m s^{-1}) is the leaf boundary layer conductance:

$$g_b = C_v \sqrt{\frac{u_*}{d_1}} \quad (24)$$

- 10 The photosynthesis-stomatal conductance model considers limitation arising from soil water stress. A soil water stress factor (β_t) scales the photosynthesis rate and stomatal conductance, being multiplied directly to A , R_d in Eq. (18) and b in Eq. (19) or Eq. (21) above to account for soil water stress (Porporato et al., 2001; Verhoef and Egea, 2014). To compute β_t , we consider a two-layer soil model consisting of a topsoil layer (0–5 cm) and a root zone beneath the top soil (5–100 cm), consistent with and constrained by the data and model structure of MERRA-2. First, the soil matric potential in each layer i , ψ_i (mm), that
 15 represents water availability in ecophysiological terms is evaluated as a function of soil wetness (s_i) and soil type:

$$\psi_i = \psi_{\text{sat},i} s_i^{-B_i} \quad (25)$$

where $\psi_{\text{sat},i}$ and B_i refer to the saturated soil matric potential and soil water characteristic parameter, respectively, both depending on soil texture. A wilting factor, w_i , is formulated as a function of ψ_i as well as ψ_c and ψ_o , which refer to the matric potential at which stomatal closure and stomatal opening occur to the full extent, respectively:

$$20 \quad w_i = \begin{cases} 1 & \text{for } \psi_i > \psi_o \\ \frac{\psi_c - \psi_i}{\psi_c - \psi_o} & \text{for } \psi_c \leq \psi_i \leq \psi_o \\ 0 & \text{for } \psi_i < \psi_c \end{cases} \quad (26)$$

The function β_t is then the average of the wilting factors weighted by the PFT-specific root fraction (r_i) in each layer:

$$\beta_t = \sum_{i=1}^2 w_i r_i \quad (27)$$

A single-layer bulk soil formulation considering only the root zone (0–100 cm) is also implemented, but is found to be inferior to the two-layer formulation in terms of reproducing observed GPP in semiarid locations (Lam and Tai, 2020).

25

The above equations calculate photosynthesis and conductance at the leaf level only, and appropriate scaling to account for vertical variation in leaf nitrogen content, light attenuation and sunlit vs. shaded leaves is needed to obtain the canopy-level photosynthesis (i.e., GPP) and conductance. This is done by scaling V_{cmax} and other parameters as follows:



$$V_{\text{cmax, sun}} = V_{\text{cmax, top}} \frac{1 - e^{-(K_n + K_b)\text{LAI}}}{K_n + K_b} \frac{1}{\text{LAI}_{\text{sun}}} \quad (28)$$

$$V_{\text{cmax, sha}} = V_{\text{cmax, top}} \left[\frac{1 - e^{-K_n \text{LAI}}}{K_n} - \frac{1 - e^{-(K_n + K_b)\text{LAI}}}{K_n + K_b} \right] \frac{1}{\text{LAI}_{\text{sha}}} \quad (29)$$

where $V_{\text{cmax, sun}}$ and $V_{\text{cmax, sha}}$ are the canopy-averaged leaf-level values for V_{cmax} for sunlit and shaded leaves, respectively, which are used to compute leaf-level photosynthesis and stomatal conductance for sunlit and shaded leaves separately (A_{sun} , A_{sha} , g_{ssun} , g_{ssha}) from the equations above; $K_n = 0.30$ is the canopy decay coefficient for nitrogen; $V_{\text{cmax, top}}$ is the PFT-specific value for V_{cmax} for the top of the canopy; K_b , LAI_{sun} and LAI_{sha} are computed from the canopy radiative transfer model (Sect. 2.2.2). Other parameters J_{max} , T_p , k_p and R_d scale similarly.

Canopy photosynthesis rate (i.e., GPP, $\mu\text{mol CO}_2 \text{ m}^{-2} \text{ s}^{-1}$) and canopy conductance (g_{can} , m s^{-1}) per unit land area of a given PFT are then:

$$\text{GPP} = A_{\text{sun}} \text{LAI}_{\text{sun}} + A_{\text{sha}} \text{LAI}_{\text{sha}} \quad (30)$$

$$g_{\text{can}} = \left(\frac{1}{g_b} + \frac{1}{g_{\text{ssun}}} \right)^{-1} \text{LAI}_{\text{sun}} + \left(\frac{1}{g_b} + \frac{1}{g_{\text{ssha}}} \right)^{-1} \text{LAI}_{\text{sha}} \quad (31)$$

The grid cell-averaged values are obtained by weighting the PFT-level values by the PFT fractional coverage of the grid cell.

2.2.4 Canopy and surface layer aerodynamics

The canopy photosynthesis and conductance calculation above require micrometeorological variables (e.g., temperature T , specific humidity q) of the canopy air as inputs. The default approach for global and regional gridded simulations is to use reanalyzed meteorological variables at 2 m above the zero-plane displacement height (i.e., $T_{2\text{m}}$, $q_{2\text{m}}$) as the proxies for canopy air conditions. The default approach for site simulations is to directly use the measured micrometeorological variables regardless of the measurement height. We also implement an option to infer canopy air conditions from micrometeorological variables at any reference height (z_{ref} , m) above the zero-plane displacement height (e.g., $z_{\text{ref}} = 10$ m in the MERRA-2 reanalysis product) based on Monin-Obukhov Similarity Theory (MOST) (Monin and Obukhov, 1954), which relates the stability of the surface layer to the generation and suppression of turbulence through the Obukhov length:

$$L_{\text{Obuk}} = \frac{-\rho c_p u_*^2 \theta}{kgH} \quad (32)$$

where ρ (kg m^{-3}) is the density of moist air (we use the value at z_{ref}), θ (K) is the potential temperature (we use $T_{2\text{m}}$ as a proxy), H (W m^{-2}) is the sensible heat flux, c_p ($\text{J kg}^{-1} \text{ K}^{-1}$) is the heat capacity of air at constant pressure, $k = 0.4$ is the von Kármán constant, and $g = 9.80616 \text{ m s}^{-2}$ is the gravitational acceleration. The friction velocity u_* (m s^{-1}) is either provided as input or inferred iteratively from the wind speed at the reference height u_{ref} (m s^{-1}):

$$u_* = k u_{\text{ref}} \left[\ln \left(\frac{z_{\text{ref}} + z_{0\text{m}}}{z_{0\text{m}}} \right) - \psi_m \left(\frac{z_{\text{ref}} + z_{0\text{m}}}{L_{\text{Obuk}}} \right) + \psi_m \left(\frac{z_{0\text{m}}}{L_{\text{Obuk}}} \right) \right]^{-1} \quad (33)$$



where z_{0m} (m) is the roughness length for momentum, and the function $\psi_m(x)$ for momentum flux follows the formulation of Zeng et al. (1998), consistent with the implementation in CLM4.5. The aerodynamic conductance (g_{ah} , $m\ s^{-1}$) for heat, water vapor and other chemical species (e.g., ozone) between the reference height z_{ref} and the surface (treated as the zero-displacement height and where the canopy air is) is then:

$$5 \quad g_{ah} = ku_* \left[\ln \left(\frac{z_{ref} + z_{0m}}{z_{0h}} \right) - \psi_h \left(\frac{z_{ref} + z_{0m}}{L_{Obuk}} \right) + \psi_h \left(\frac{z_{0h}}{L_{Obuk}} \right) \right]^{-1} \quad (34)$$

where z_{0h} (m) is the roughness length for heat, water vapor and other chemical species, and the function $\psi_h(x)$ for heat and other material fluxes also follows the formulation of Zeng et al. (1998). Canopy air potential temperature (θ_a , K) and specific humidity (q_a , $kg\ kg^{-1}$) can then be inferred as:

$$\theta_a = \theta_{ref} + \frac{H}{\rho c_p g_{ah}} \quad (35)$$

$$10 \quad q_a = q_{ref} + \frac{E}{\rho g_{ah}} \quad (36)$$

where θ_{ref} (K) and q_{ref} ($kg\ kg^{-1}$) are the potential temperature and specific heat capacity at z_{ref} , and E ($kg\ m^{-2}\ s^{-1}$) is the evapotranspiration flux.

For the computation of ozone damage and dry deposition fluxes (Sect. 2.2.5, 2.2.6), g_{ah} is also needed and computed either using the default formulation above, or an alternative formulation that is consistent with the default dry deposition scheme in GEOS-Chem (Wesely, 1989; Wang et al., 1998).

2.2.5 Ozone damage

Two ozone (O_3) damage schemes are implemented in TEMIR, which considers the responses of vegetation in terms of photosynthesis and stomatal conductance. The first O_3 damage scheme follows Sitch et al. (2007) and considers two levels of O_3 sensitivity (high and low) for each of the five major plant groups, namely, “broadleaf”, “needleleaf”, “shrub”, “C3 grass”, “C4 grass” as defined by Karlsson et al. (2004) and Pleijel et al. (2004). These groups are mapped to the default TEMIR PFTs accordingly. The scheme represents O_3 damage by an O_3 impact factor (f) that is dependent on the instantaneous stomatal O_3 flux into the leaf interior:

$$25 \quad f = 1 - a \max \left[\left(\frac{[O_3]}{g_{ah}^{-1} + g_b^{-1} + k_{O_3} g_s^{-1}} - F_{crit} \right), 0 \right] \quad (37)$$

where $[O_3]$ ($nmol\ m^{-3}$) is the O_3 concentration observed or of the lowest atmospheric model layer; the aerodynamic, leaf boundary layer and stomatal conductances are calculated using the formulations in the previous sections; $k_{O_3} = 1.67$ as defined by Sitch et al. (2007) is the ratio of the leaf resistance for O_3 to that for water vapor; F_{crit} represents a critical threshold accounting for O_3 tolerance, below which instantaneous O_3 exposure does not affect photosynthesis, and $F_{crit} = 1.6\ nmol\ m^{-2}\ s^{-1}$ for woody PFTs and $F_{crit} = 5\ nmol\ m^{-2}\ s^{-1}$ for grass PFTs; the O_3 sensitivity parameter a ($nmol^{-1}\ m^2\ s$) is specific to the plant group and to the two levels of O_3 sensitivity. Factor f is multiplied directly to the net photosynthesis rate A_n to represent



O₃ damage, which then indirectly affects g_s via the coupling between A_n and g_s ; since the calculation of f requires g_s , the three variables f , A_n and g_s need to be solved together by numerical iterations. Noniterative methods give insignificant differences in performance.

The second scheme follows Lombardozzi et al. (2012, 2015) scheme and considers three O₃ sensitivity levels (high, average and low) for each of the three major plant groups, namely, “broadleaf”, “needleleaf” and “grasses and crops”, which are mapped to the default TEMIR PFTs accordingly. Unlike the Sitch et al. (2007) scheme, O₃ damage is characterized by the cumulative uptake of O₃ (CUO, mmol m⁻²) instead of instantaneous O₃ uptake, which is parameterized as the sum of the instantaneous stomatal O₃ flux over the lifetime of the leaf:

$$CUO = 10^{-6} \sum \left(\frac{[O_3]}{g_{ah}^{-1} + g_b^{-1} + k_{O_3} g_s^{-1}} - F_{crit} \right) \Delta t \quad (38)$$

where Δt (s) is the model timestep; the critical threshold to account for O₃ tolerance is set to be $F_{crit} = 0.8$ nmol m⁻² s⁻¹ and CUO is only calculated when the LAI of the PFT concerned is larger than 0.5 to avoid unrealistically high CUO (Lombardozzi et al., 2012). Another important difference from (Sitch et al., 2007) is that O₃ damage alter photosynthesis and stomatal conductance separately using two different sets of O₃ impact factors, f_p and f_c , respectively:

$$f_p = a_p CUO + b_p \quad (39)$$

$$f_c = a_c CUO + b_c \quad (40)$$

where the intercepts b_p , b_c and slopes a_p , a_c are determined empirically for the three plant groups (Lombardozzi et al., 2015). Factors f_p and f_c are multiplied separately to A_n and g_s , respectively, after the iterative calculation of A_n and g_s .

2.2.6 Dry deposition

We implement two major dry deposition schemes: Zhang et al. (2003) scheme used in several Canadian and American air quality models, and Wesely (1989) scheme widely used in many chemical transport models including WRF-Chem and GEOS-Chem. In each of the two schemes, the default stomatal conductance scheme is a semi-empirical formulation that is not coupled to plant ecophysiology; the default canopy radiative transfer and aerodynamic conductance also follow formulations that are different from the default TEMIR schemes described above. We implement options such that ecophysiology-based stomatal conductance (g_s) computed from the photosynthesis model above (Sect. 2.2.3), as well as canopy radiative transfer (ϕ_{sun} , ϕ_{sha} , LAI_{sun}, LAI_{sha}; Sect. 2.2.2) and aerodynamic conductance (g_{ah} ; Sect. 2.2.4), can be used to replace the default options in the dry deposition schemes. A full evaluation of dry deposition velocities and fluxes computed by TEMIR using different combinations of schemes against O₃ flux observations has been conducted by Sun et al. (2022). Tai et al. (2021) also evaluated how the dry-depositional fluxes of O₃ can affect global crop yields by integrating TEMIR with the Deposition of O₃ for Stomatal Exchange (DO₃SE) model (<https://www.sei.org/projects-and-tools/tools/do3se-deposition-ozone-stomatal-exchange/>).



3 Observational datasets for model evaluation

3.1 Site-level dataset

Site-level comparison utilizes the eddy covariance measurements from the flux tower sites of the FLUXNET network (<https://fluxnet.fluxdata.org>). The latest released dataset, FLUXNET2015, contains half-hourly or hourly measurements of carbon fluxes and various meteorological observations. Each site is classified to contain one PFT that follows the classes described in the International Geosphere Biosphere Program Data and Information System (IGBP-DIS) DISCover land cover dataset (Loveland and Belward, 1997).

Data after year 2009 from FLUXNET is used for model validation, taking into account data quality using the FLUXNET quality flags for each meteorological variable measured. TEMIR follows the PFT classes of CLM4.5, which are defined differently to the IGBP-DIS scheme, so additional identification and matching of the PFT classes is performed based on the forest composition information provided as far as possible in the FLUXNET database, as shown in Table S1 in the Supplemental Information. Overall, five sites have mismatched PFTs where the TEMIR outputs do not contain the corresponding PFT classes specified by FLUXNET. Thus, a total of 49 sites were used for comparison as listed in Table S2 whereby most are in the Northern Hemisphere. 14 sites are evergreen needleleaf forests (ENF), 2 are evergreen broadleaf forests (EBF), 6 are deciduous broadleaf forests (DBF), which together account for almost half of the total number of sites. The rest of the 27 sites are 1 open shrubland (OSH), 16 grasslands (GRA) and 10 croplands (CRO). The GPP products provided by FLUXNET are derived by partitioning from the net ecosystem exchange (NEE) that is directly measured by the flux towers, using two partitioning methods: one utilizing daytime data only as described by Lasslop et al. (2010) and the other utilizing the nighttime approach according to Reichstein et al. (2005). A major difference in the GPP products partitioned using these two methods is that the nighttime approach for some extreme events such as droughts gives negative GPP, which is not physical. The NEE of the dataset is also produced using two methods that consider constant vs. variable friction velocity thresholds to filter NEE accordingly. The FLUXNET GPP product used in our comparison is the mean GPP product partitioned using the daytime method with the variable friction velocity threshold denoted as GPP_DT_VUT_MEAN in the FLUXNET database.

3.2 Global-scale dataset

We use the solar-induced induced chlorophyll fluorescence (SIF) inferred GPP product derived by Li and Xiao (2019) for global validation. SIF-based GPP products rely on the correlation of SIF with GPP where there is a good representation (e.g., Shekhar et al., 2022). The global GPP dataset derived by Li and Xiao (2019) is based on the global SIF product from Orbiting Carbon Observatory-2 (OCO-2), namely GOSIF, and on the relationships between SIF and site-level observed GPP (Li et al.,



2018). The resulting dataset has a spatial resolution of 0.05° and a monthly temporal resolution. For model validation, GOSIF GPP is regridded to a resolution of $2^\circ \times 2.5^\circ$ and grid cells with zero GPP are excluded.

4 Model and simulation setup

4.1 Site-level simulations with TEMIR

5 For each of the 49 FLUXNET sites (Table S2) beginning from year 2009, simulations shown in Table 1 are conducted for model-observation comparison, with ambient CO_2 concentration kept constant at 390 ppmv. The first is to use the default meteorological fields prescribed from MERRA-2 at $2^\circ \times 2.5^\circ$ horizontal resolution consistent with the GEOS-Chem simulations described above. We also test turning on and off the option of using MOST to infer in-canopy micrometeorological variables from the prescribed meteorology at 2 m above displacement height, as described in Sect. 2.2.4. The second set is to use direct
10 micrometeorological measurements available from the FLUXNET site towers as the driving meteorology and the default MERRA-2 meteorology used only to replace any missing or low-quality data. The results simulated are most relevant for evaluating model performance in reproducing the observed diurnal and seasonal cycle of GPP from each FLUXNET site.

Table 1: TEMIR simulation settings for selected FLUXNET sites.

Simulation	Meteorology	Monin-Obukhov (MOST) Setting
TEMIR_FLUX	FLUXNET	Off
TEMIR_MO_off	MERRA-2	Off
TEMIR_MO_on	MERRA-2	On

15

4.2 Global simulations with TEMIR

Global simulations from 2010 to 2015 are conducted under the same general setup as the site-level simulations, with ambient CO_2 concentration fixed at 390 ppmv and driven by $2^\circ \times 2.5^\circ$ MERRA-2 meteorology. Functionalities of the model are tested for performance, as shown in Table 2, the MOST option to infer in-canopy conditions and the Sitch O_3 damage scheme with
20 low and high sensitivity to assess the global O_3 impact on vegetation. We use GEOS-Chem (Sect. 2.1) to simulate tropospheric O_3 , starting from year 2009 to 2015 whereby the first year of simulation is considered as spin-up. The simulation uses the comprehensive chemistry scheme “tropchem”, which has tropospheric O_3 - NO_x -VOC-aerosol chemistry accompanied by the default emission inventories (i.e., anthropogenic emissions from CEDS; Hoesly et al., 2018, and biogenic emissions from MEGAN; Guenther et al., 2012). The reanalyzed meteorological fields used are from the Modern Era-Retrospective Analysis
25 for Research and Applications version 2 (MERRA-2) supplied by the Global Modeling and Assimilation Office (GMAO) at $2^\circ \times 2.5^\circ$ horizontal resolution, which are the identical meteorological inputs used in TEMIR. Simulated O_3 concentrations at



the lowest surface level are then fed into TEMIR as inputs accordingly. The results produced from these simulations (Table 2) are used to validate the spatial variability of seasonal and annual averages across the whole world against the GOSIF GPP dataset (Sect. 3.2). To retain representative results from all simulations (Table 2), grid cells with LAI < 0.5 are excluded. LAI dataset for the simulation is from MODerate resolution Imaging Spectroradiometer (MODIS) satellite data (Lawrence and Chase, 2007) and assimilated by Yuan et al. (2011).

Table 2: TEMIR simulation settings for global simulation for years 2010–2015.

Simulation	Sitch O ₃ Damage Scheme Sensitivity	Monin-Obukhov (MOST) Setting
TEMIR_MO_off	Off	Off
TEMIR_MO_on	Off	On
TEMIR_SI	Low	Off
TEMIR_Sh	High	Off

4.2.1 Global CO₂-O₃ factorial simulations with TEMIR

We perform factorial simulations (Table 3) to investigate the effects of CO₂ fertilization, O₃ damage and their interactions on global primary productivity as an example to showcase the utility of the model. Global O₃ surface concentrations of year 2000 are simulated using GEOS-Chem (Sect. 2.1) with year 1999 used as spin up; other settings are as described in Sect. 4.2. CO₂ concentrations are changed in TEMIR as required for each simulation (Table 3) with reference to year-2000 and year-2010 concentrations (Dlugokencky and Tans, 2022). Sitch O₃ damage scheme with high sensitivity is used for TEMIR simulations (Table 3) when global surface O₃ concentrations are used as inputs; otherwise no O₃ damage scheme is used. Year-2000 meteorological fields MERRA-2 are used for all GEOS-Chem and TEMIR simulations. LAI is fixed at year 2000 from MODIS for all GEOS-Chem and TEMIR simulations.

Table 3: Factorial simulation settings. “N/A” for O₃ year indicates that no O₃ damage scheme is used.

Simulation	CO ₂ (ppmv)	O ₃ Year	Meteorology Year
C0_O0	370	N/A	2000
C1_O0	390	N/A	
C0_O1	370	2000	
C1_O1	390	2000	



5 Model evaluation

Statistics used for model validation are the adjusted coefficient of determination R^2 , the modified Nash–Sutcliffe model efficiency coefficient N and the normalized mean bias B . R^2 is a commonly used metric with a range of 0 to 1 (or 0–100%) that represents the fraction of variability of observations that can be replicated by the model, whereby 1 indicates perfect correlation and 0 indicates no correlation. N addresses the sensitivity issues of R^2 documented by Legates and McCabe (1999). With values from negative infinity to 1, it is a measure of the suitability of the model as a predictor instead of using the mean of the observations. When $N = 1$, it indicates that the model perfectly replicates observations, and no preference is observed between the model and the mean of the observations as a predictor. Negative values in turn signify the incapability of the model in predicting system behaviors. B gives the relative difference of the magnitude of model results from the observations. The equations to compute these statistics are shown in Table 4 below.

Table 4: Statistical metrics for TEMIR model validation, where M and O respectively represent the simulated dataset and observational dataset, each containing n data points. \bar{M} and \bar{O} represent the means of the datasets in question.

Metric	Mathematical equation	Range
Coefficient of Determination R^2	$R^2 = \left(\frac{\sum_{i=1}^n (M_i - \bar{M})(O_i - \bar{O})}{\sqrt{\sum_{i=1}^n (M_i - \bar{M})^2 \sum_{i=1}^n (O_i - \bar{O})^2}} \right)^2$	0 to 1 (0 to 100%)
Modified Nash–Sutcliffe Model Efficiency Coefficient N	$N = 1 - \frac{\sum_{i=1}^n O_i - M_i }{\sum_{i=1}^n O_i - \bar{O} }$	$-\infty$ to 1
Normalized Mean Bias B	$B = \frac{\bar{M}}{\bar{O}} - 1$	$-\infty$ to ∞

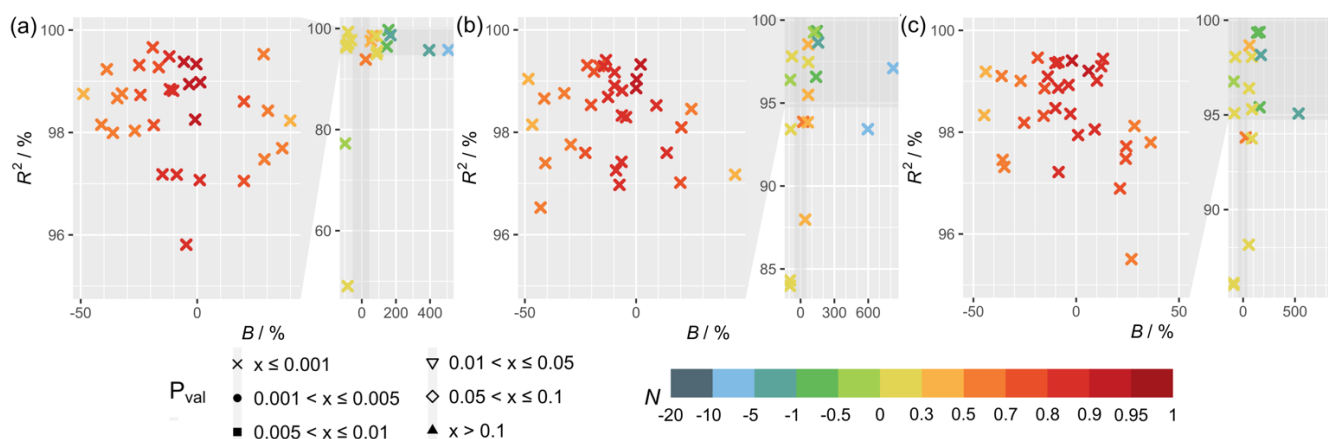
5.1 Site-level validation

5.1.1 Validation on summer diurnal cycle

Figure 1 shows the statistical metrics (Table 4) used to perform model-observation comparison for the diurnal GPP cycle calculated for each FLUXNET site taken from the second summer month of year 2012, which corresponds to the month of July for sites in the Northern Hemisphere and January in the Southern Hemisphere (Table S2). Comparing between the simulations with FLUXNET local meteorology and MERRA-2 meteorology (Figure 1), statistical metrics generally do not differ substantially, but some significant differences can exist for some sites (e.g., CH-Cha, CH-Dav; see Figure 3) where results from simulations with FLUXNET local meteorology show higher correlations. For simulations solely driven by



MERRA-2 meteorology, inferring in-canopy meteorology using Monin-Obukhov similarity theory (Figure 1(c)) gives insignificant differences for all sites.



5 **Figure 1: Statistical metrics (Table 4) for model-observation comparison for diurnal gross primary product (GPP) from simulations (a) TEMIR_FLUX, (b) TEMIR_MO_off and (c) TEMIR_MO_on as described in Table 1.**

Figure 2 shows the statistical metrics (Table 4) for model-observation comparison for the simulations using FLUXNET local meteorology as the driving meteorological input for different PFTs. The average correlations per PFT between observed and simulated GPP (Figure 2) are high ($R^2 > 0.88$), except for open shrubland ($R^2 \approx 0.7$). B shows a large variability due to various limitations of the model for each PFT. For forest sites, B generally has a smaller range and lower absolute mean values in comparison to the other PFTs, showcasing the better performance of TEMIR for forests. N shows similar behaviors, namely, the prediction for forest sites is satisfactory with mean values of N larger than 0.55, whereas N is mostly negative for grasslands, croplands and open shrublands. All plots of diurnal cycles are shown in the Supplementary Materials, with relevant figures also included in the following discussion.

10

15

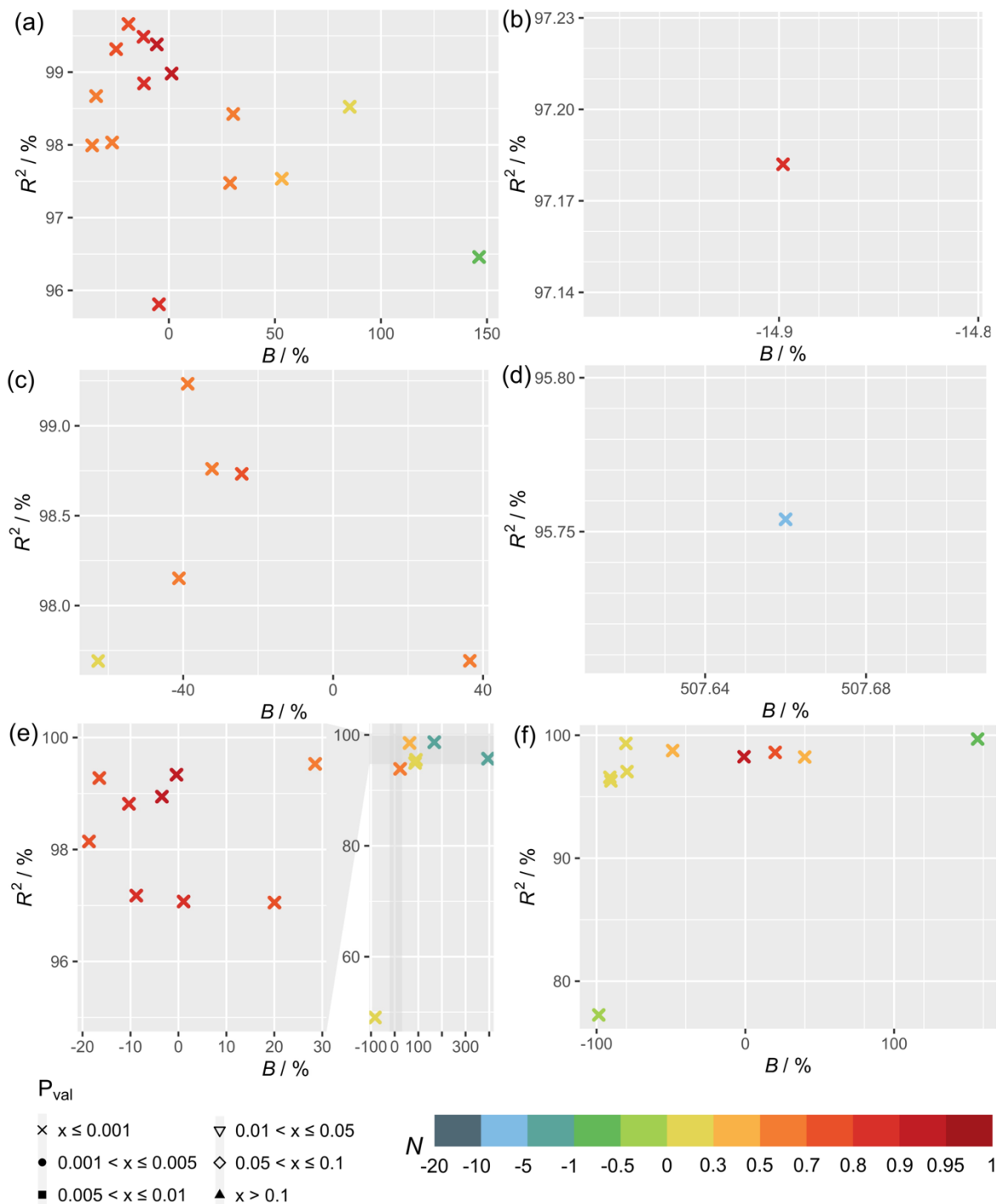


Figure 2: Statistical metrics (Table 4) for model-observation comparison for diurnal gross primary product (GPP) from TEMIR_FLUX simulation (Table 1) for each plant functional type (PFT) listed in Table S1: (a) evergreen needleleaf forest (ENF), (b) evergreen broadleaf forest (EBF), (c) deciduous broadleaf forest (DBF), (d) open shrubland (OSH), (e) grassland (GRA), (f) cropland (CRO).

5



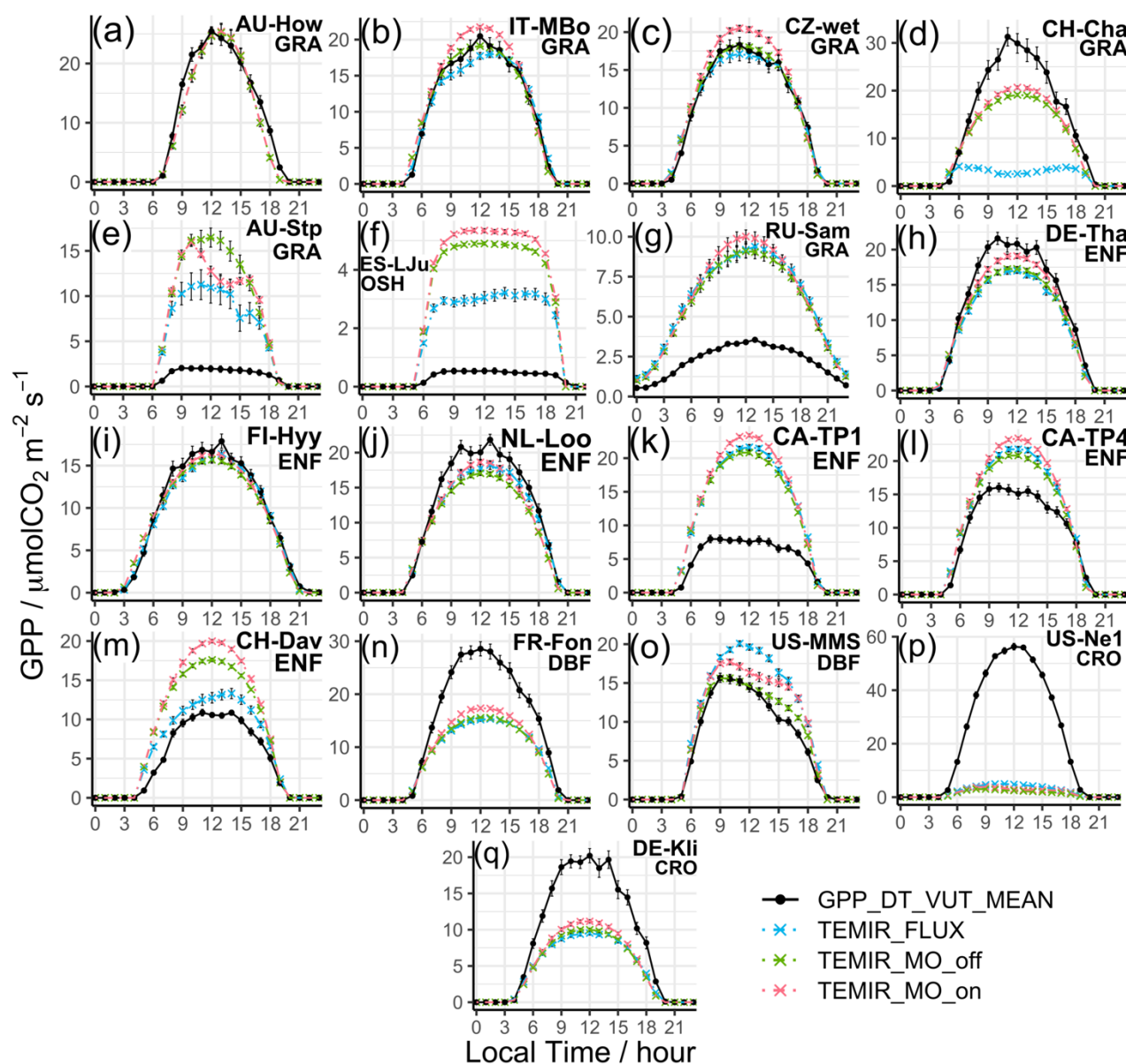
We find that the correlations are above 90% (Figure 2(e)) for all grassland sites (e.g. AU-How, Figure 3(a); IT-MBo, Figure 3(b); CZ-wet, Figure 3(c)) except for CH-Cha (Figure 3(d)) where FLUXNET meteorology gives $R^2 = 0.49$, likely due to disturbances from intensive site management (Imer et al., 2013). Yet the spread of B is large, where we see absolute B values greater than +0.6 and the rest with absolute B less than 0.3 for six of the 16 sites. A possible explanation for the high B values is the fire-prone nature of these sites (i.e., AU-Stp, Figure 3(e)) (Beringer et al., 2007, 2011; Hutley et al., 2011; Haverd et al., 2013) whereby the model is incapable of resolving such complexities as turnover and local disturbances. Another cause of overestimation is the simplistic and generic PFT classification for such biomes, which are usually sparsely populated yet with much diversity, as in the open shrubland site ES-LJu (Figure 3(f)) (Serrano-Ortiz et al., 2009). Such generalization can also cause systematic inaccuracies in parameterization, where model parameters are better suited for European semiarid vegetation (e.g., CH-Fru (Imer et al., 2013); IT-MBo, Figure 3(b) (Marcolla et al., 2011); CZ-wet, Figure 3(c) (Dušek et al., 2012)) than similar sites of other regions (e.g., AU-Dry (Hutley et al., 2011); RU-Sam, Figure 3(g) (Boike et al., 2013); US-SRG (Scott et al., 2015)).

Simulated results for forest PFTs compare very well with observations, where N values are often greater than 0.5. TEMIR performs particularly well for evergreen needleleaf forests as seen in sites DE-Tha (Figure 3(h)), FI-Hyy (Figure 3(i)) and NL-Loo (Figure 3(j)), which are mostly populated by mature Scots pine forests of over 70 years old. Sites CA-TP1 (Figure 3(k)), CA-TP3 (Peichl et al., 2010; Arain et al., 2022) and DE-Lkb (Lindauer et al., 2014) are overestimated by the model as these forests are dominated by eastern white pine and Norway spruce that are less than 20 years old, so optimal productivity might not have been achieved. In comparison, the neighboring site CA-TP4 (Figure 3(l); Peichl et al., 2010) with over 70-year-old eastern white pine is better replicated by the model. The model has better performance with respect to site observations when using FLUXNET local meteorology (e.g., CH-Dav, Figure 3(m); Zielis et al., 2014), though the differences are insignificant for most sites. For deciduous broadleaf forest sites, although represented well overall, there is a systematic underestimation (e.g., FR-Fon, Figure 3(n)), most likely due to inaccurate parameterization overcompensating for the uncertainties of satellite-derived LAI for broadleaf trees. The multi-year drought in the US over the 2010s, which hinders plant productivity (Wolf et al., 2016; Xu et al., 2020), appears to improve model agreement by reducing the discrepancy (i.e., US-Oho and US-UMB) and even giving a positive model bias (i.e., US-MMS, Figure 3(o); Yi et al., 2017).

The correlation for croplands is high but there is a spread in B giving varying N values. The range of model performance among cropland sites shows the limitation of the simplistic crop representation used in this version of TEMIR, whereby site-level settings such as planting seasons and agricultural management (e.g., fertilizer usage, irrigation and possible rotations between crop types and cultivars) are not considered. The generic crop representation fails to capture the maximum photosynthetic capacity of the planted crops. For example, site US-Ne1 has irrigated maize that has much higher GPP



compared to the simulated generic crop as shown in Figure 3(p); site DE-Kli (Figure 3(q)) has a 5-year crop rotation with occasional fertilizer application (Prescher et al., 2010) and has higher productivity than simulated by the model.

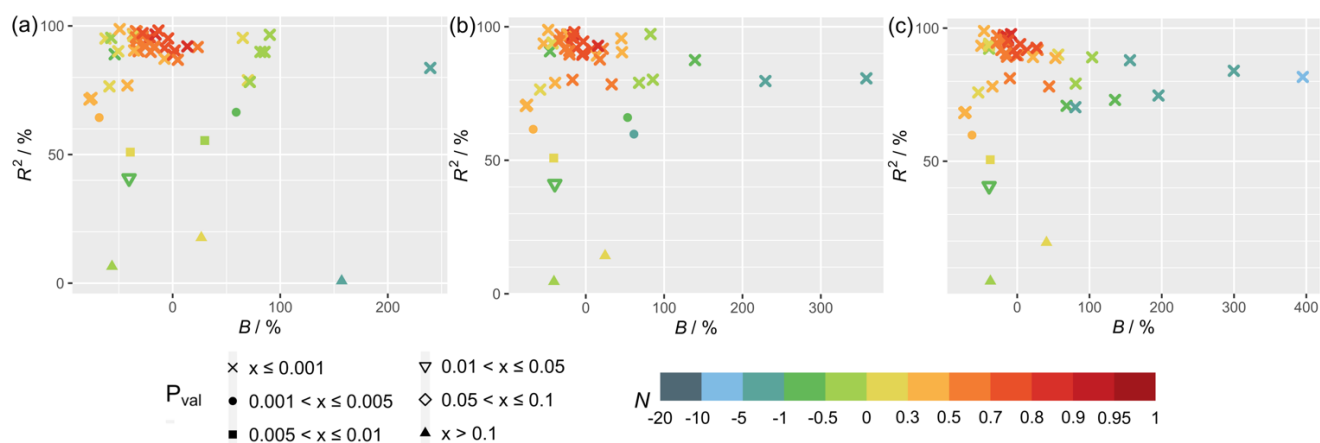


5 **Figure 3: Diurnal averaged gross primary productivity of selected sites representative of their respective vegetation types (a) AU-How, (b) IT-MBo, (c) CZ-wet, (d) CH-Cha, (e) AU-Stp, (f) ES-LJu, (g) RU-Sam, (h) DE-Tha, (i) FI-Hyy, (j) NL-Loo, (k) CA-TP1, (l) CA-TP4, (m) CH-Dav, (n) FR-Fon, (o) US-MMS, (p) US-Ne1, and (q) DE-Kli from simulations described in Table 1 with relevant site information annotated. More details of these sites are given in Table S2.**



5.1.2 Validation on seasonal cycle

Figure 4 shows the statistical metrics (Table 4) for monthly GPP averages of 2009–2013 to examine the model performance in seasonal GPP cycle. All plots of monthly cycles are shown in the Supplementary Materials, with plots of selected sites included in the following discussion. The model generally performs worse in capturing the seasonal cycle than the diurnal cycle. Between the different settings of meteorology used for simulations (Figure 4), the differences in statistics are small. MERRA-2 meteorology shows good utility for most sites, with in-canopy meteorology inferred using Monin-Obukhov similarity theory improving correlation for some sites. FLUXNET local meteorology gives the smallest range of biases with performance similar to MERRA-2 meteorology simulations.



10

Figure 4: Statistical metrics (Table 4) of monthly gross primary product (GPP) from simulations (a) TEMIR_FLUX, (b) TEMIR_MO_off and (c) TEMIR_MO_on as described in Table 1.

Comparing Figure 2 and Figure 5, model-observation comparison of monthly averages gives lower values of R^2 for all sites in general. On the other hand, biases are distributed more evenly across the range with smaller extreme values compared to the biases from diurnal simulations. In terms of N , the model is less adept in reproducing seasonal variations (due to the reductions in correlation) regardless of the driving meteorology chosen. Figure 5(c) shows that deciduous broadleaf sites (e.g., US-MMS; Figure 6(a)) gives $R^2 > 0.85$ with the maximum absolute $B = +0.54$, and minimum $N = 0.42$ with a mean of 0.9. Monthly performance of forest sites shows a smaller range in B and lower absolute mean values of B in comparison to the other PFTs (Figure 5). The prediction for forest sites is satisfactory with mean values of N larger than 0.65 (e.g., RU-Fyo in Figure 6(b); CA-TP4 in Figure 6(c)), and monthly GPP inaccuracies for forest sites can be explained with similar reasoning as discussed in Sect. 5.1.1.

The correlation for grasslands is above 75% for most sites (e.g., DE-Akm in Figure 6(d); IT-MBo in Figure 6(e)) while sites AU-How (Figure 6(f)) and AU-Stp have R^2 below 0.4. These sites are known to have fires occurring in the dry winter and

25



spring from May to October, which corresponds to the low productivities (Beringer et al., 2007, 2011; Hutley et al., 2011; Haverd et al., 2013). Moreover, such disturbances on LAI with vegetation regrowth are complex and often overlooked by the model as shown in simulation of site AU-How with minimal productivity.

- 5 The simulation of monthly GPP of croplands shows most clearly the limitations of the generic model approach, as no site-specific crop phenology is available in this version of the model. The simulated seasonal cycle shows a typical annual peak usually in summer as dictated by meteorology that in general can yield good correlation (e.g., DE-Geb, Figure 6(g)); yet as many sites are intensively managed, the observed GPPs do not follow such simplistic cycle, giving low correlations (e.g., IT-BCi, Figure 6(h)). The parameters for generic crop usually fail to represent the actual crop planted at the sites, and therefore
- 10 large biases exist in the simulated GPP (e.g., BE-Lon in Figure 6(i)); FR-Gri in Figure 6(j)). GPP is more commonly underestimated in the US sites (e.g., US-Ne1 in Figure 6(k)) where maize is usually planted and is more productive in comparison to other crops.

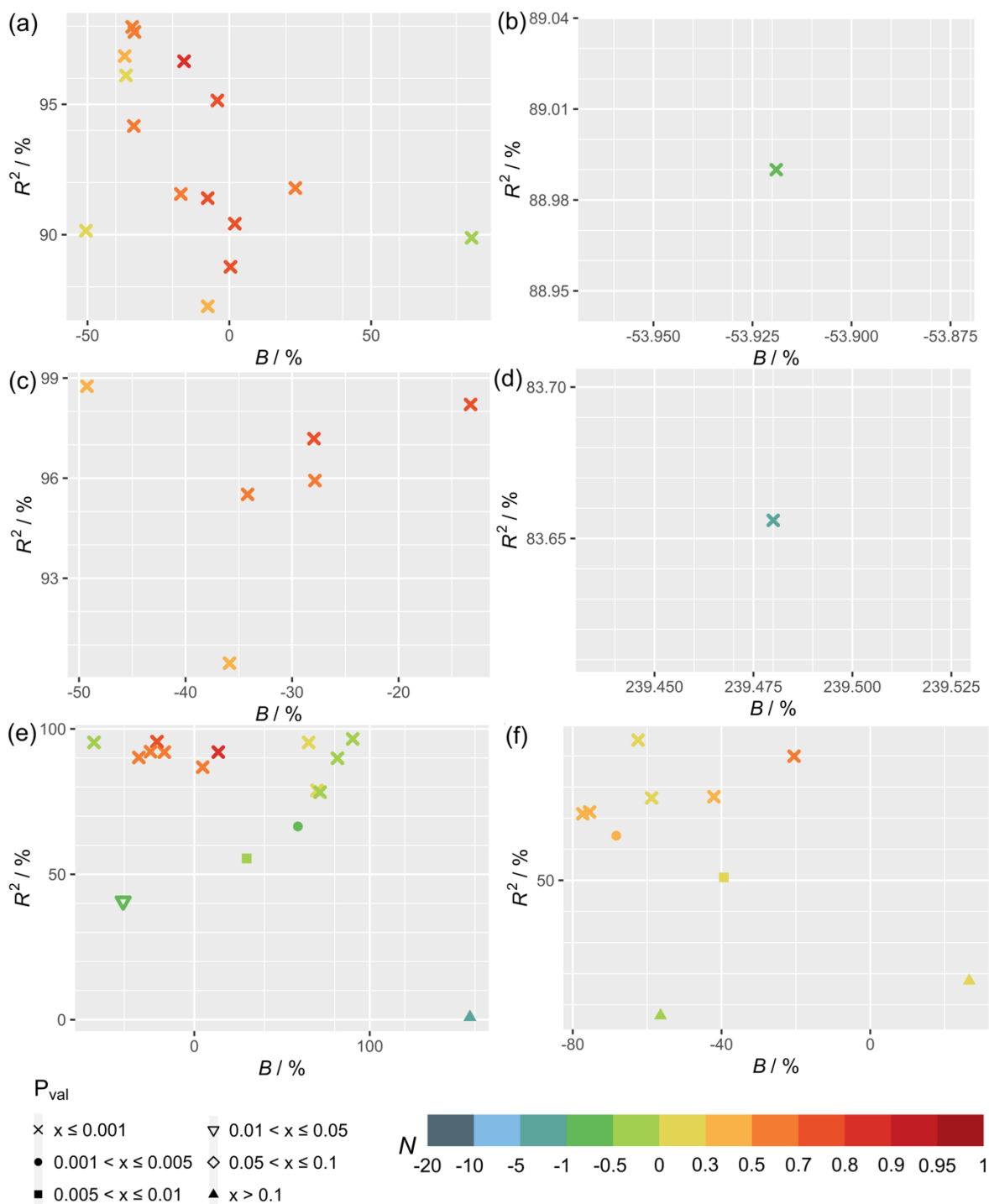
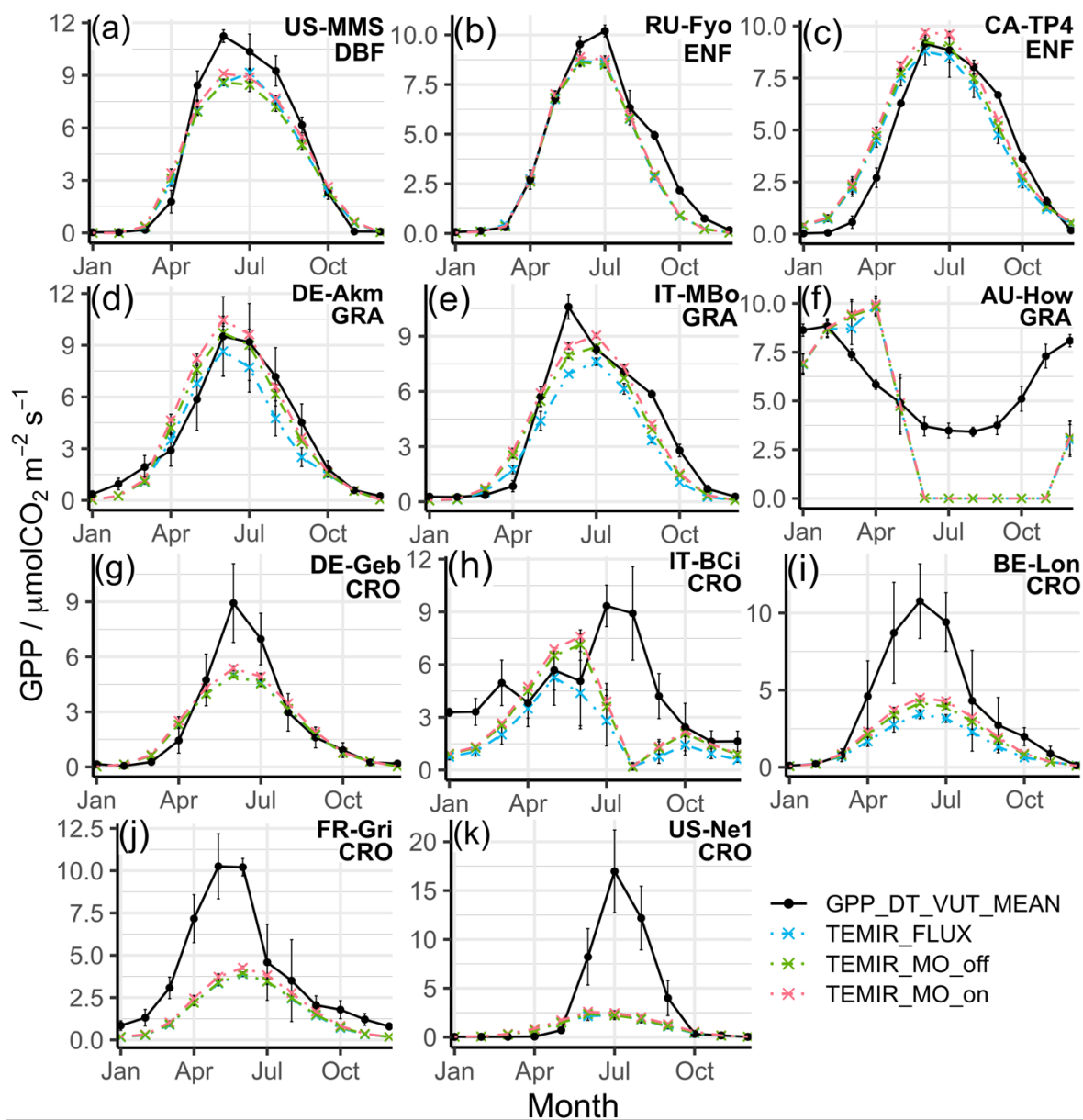


Figure 5: Statistical metrics (Table 4) of monthly averaged gross primary product (GPP) from TEMIR_FLUX simulation (Table 1) for each plant functional type (PFT) listed in Table S1: (a) evergreen needleleaf forest (ENF), (b) evergreen broadleaf forest (EBF), (c) deciduous broadleaf forest (DBF), (d) open shrubland (OSH), (e) grassland (GRA), (f) cropland (CRO).



5 **Figure 6: Monthly averaged gross primary productivity of selected sites representative of their respective vegetation types: (a) US-MMS, (b) RU-Fyo, (c) CA-TP4, (d) DE-Akm, (e) IT-MBo, (f) AU-How, (g) DE-Geb, (h) IT-BCi, (i) BE-Lon, (j) FR-Gri, and (k) US-Ne1 from simulations described in Table 1 with relevant site information annotated.**



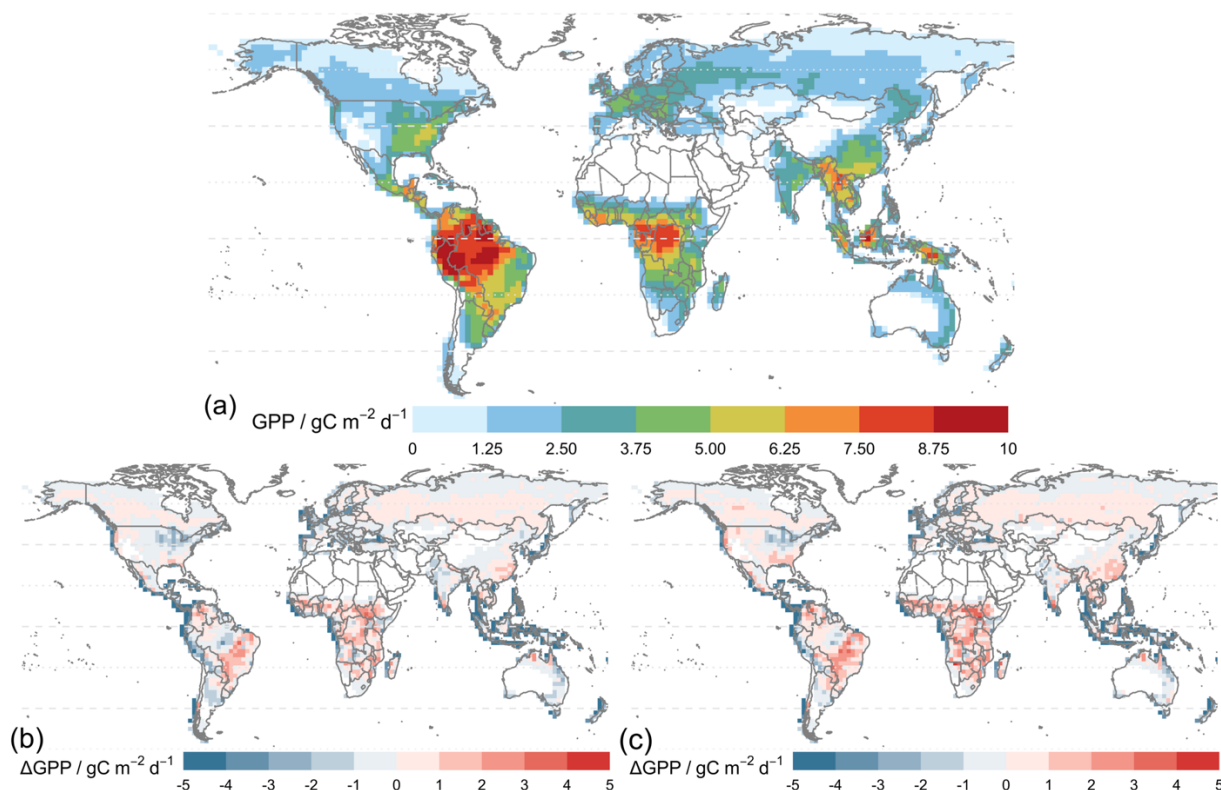
5.2 Global validation

Figure 7 shows that simulated annual averaged GPP of years 2010–2015 is 134.7 Pg C yr⁻¹ from the simulation using MERRA-2 meteorology (TEMIR_MO_off) (Figure 7(b)), and the simulation with in-canopy meteorology inferred using MOST (TEMIR_MO_on) gives GPP over the same period to be 144.7 Pg C yr⁻¹ (Figure 7(c)). Comparing to the satellite-derived dataset (GOSIF GPP; Sect. 3.2) where annual GPP of the same period being 128.4 Pg C yr⁻¹ (Figure 7(a)), TEMIR overestimates global GPP by ~5–10% depending on the input meteorology (Table 5). TEMIR performance is well within and leans toward the middle of the observation-constrained range in the literature of 119–175 Pg C yr⁻¹. TEMIR closely agrees with models of similar design objectives, e.g., the Yale Interactive terrestrial Biosphere (YIBs) with GPP at 125 ± 3 Pg C yr⁻¹ (Yue and Unger, 2015) and JULES land surface model estimating GPP at 141 Pg C yr⁻¹ (Slevin et al., 2017). TEMIR can largely reproduce the spatial distribution of GPP with respect to GOSIF GPP (Figure 7), with grid cells with mixed savanna and forests showing larger discrepancies.

Table 5: Gross primary product (GPP) simulated and relevant simulations details of global TEMIR simulations described in Table 2 and Table 3 (“N/A” for O₃ year indicates that no O₃ damage scheme is used).

Simulation	Simulation Year(s)	CO ₂ (ppmv)	O ₃ Year	GPP (Pg C yr ⁻¹)
TEMIR_MO_off	2010–2015	390	N/A	134.7
TEMIR_MO_on		390	N/A	144.7
TEMIR_Sl		390	2000	133.6
TEMIR_Sh		390	2000	131.8
C0_O0	2000	370	N/A	135.2
C1_O0		390	N/A	138.6
C0_O1		370	2000	132.7
C1_O1		390	2000	136.2

Figure 8 shows model-observation statistics (Table 4) for the model outputs of Figure 7 in 12 regions. Global correlation of 6-year averaged GPP is around 83% (Figure 8(b)). In general, correlations are lower for regions closer to the equator, where correlations for tropical regions are below 70%, but otherwise above 70% with correlation for Siberia close to 90%. Correlation for Tropical Americas is ~75%, which is higher than other equatorial regions. Temperate North America shows a correlation of ~60%, which is slower than other regions at midlatitudes. We also see that GPP is underestimated in the grid cells with high crop density (Figure 7(b)), which, as discussed in Sect. 5.1, is likely due to the generic crop representation of the TEMIR version giving poor model performance for this region. Simulated GPP driven by meteorology inferred with MOST gives small increases or decreases in regional correlation (e.g., correlation for North Africa and Middle East drops from 48% to 45% and correlation for Temperate South America increases from 75% to 78%).



5 **Figure 7: (a) Average global gross primary product (GPP) of year 2010 to 2015 from GOSIF GPP product and differences in simulated GPP from simulations (b) TEMIR_MO_off or (c) TEMIR_MO_on (Table 1) of year 2010 to 2015 compared to the GOSIF product.**

Absolute biases are mostly within 25% except for North Africa and Middle East and Sub-Saharan Africa (except Central Africa) when the driving meteorology is inferred from MOST. Simulated GPP driven by in-canopy meteorology inferred with MOST gives more positive biases for all regions, generally around +10%. GPP for 6 of the 12 regions are overestimated by TEMIR and otherwise underestimated (Figure 8(b)). Thus, in-canopy meteorology inferred with MOST results in regional bias changes from underestimation to overestimation for East and South Asia, Europe, Temperate North America, and Tropical Americas. The bias for Europe is -6.2% and +1.19% when driving meteorology is inferred with MOST. The bias of +1.19% is the smallest absolute bias of any region, which shows the possibility of in-canopy meteorology inferred with MOST improving GPP predictions for some but not all regions.

10

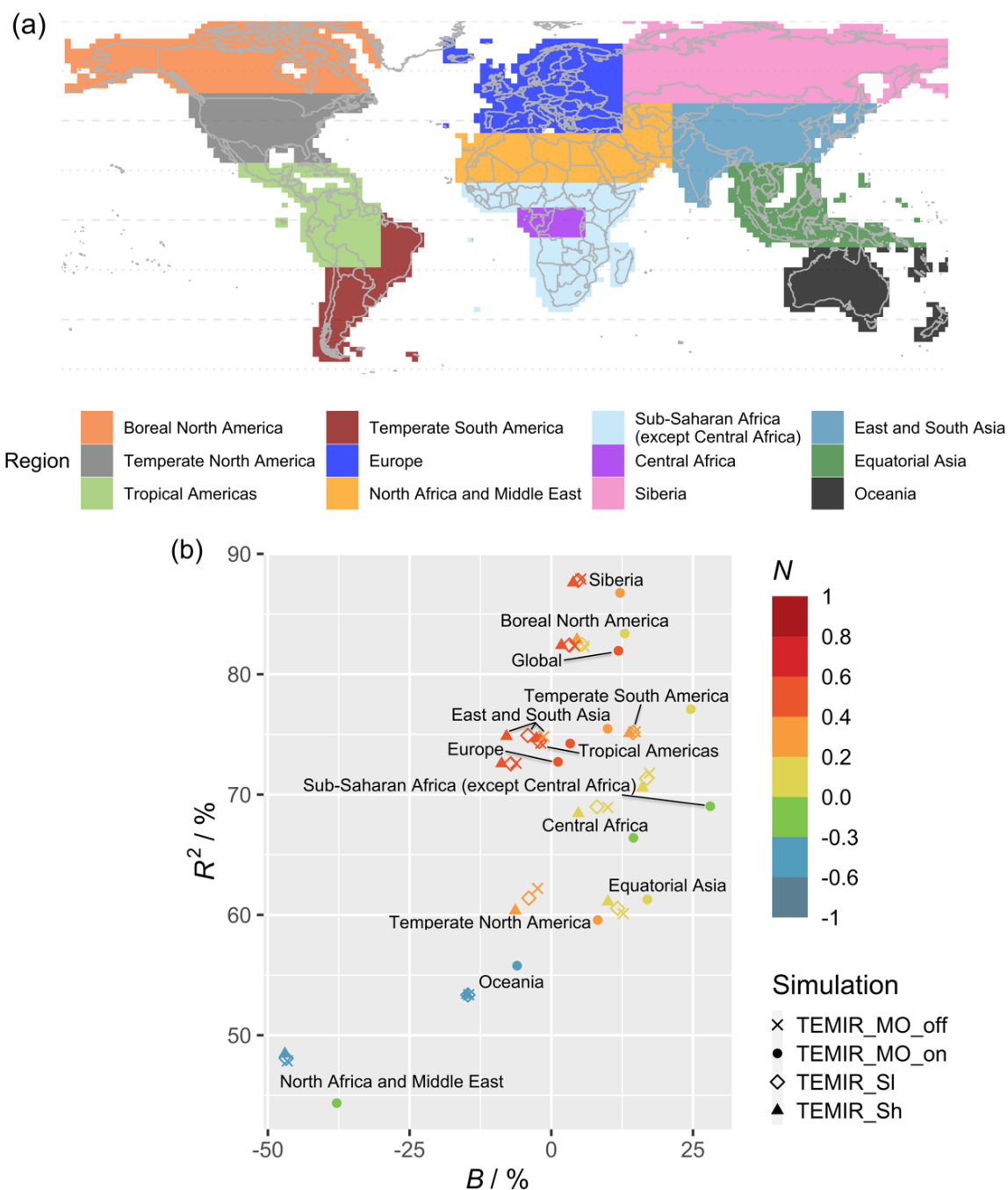


Figure 8: (a) Regional division relevant for this study largely following Chen et al. (2017), and (b) the corresponding regional statistical metrics (Table 4) of averaged gross primary product (GPP) for years 2010–2015 from TEMIR simulations (Table 2).



5.3 Effects of O₃ and CO₂ on global primary productivity

Figure 9 shows the simulated results where the Sitch O₃ scheme (Sect. 2.2.5) of low sensitivity (Sl) and high sensitivity (Sh) are implemented for the years 2010–2015 using MERRA-2 meteorology. Figure 9(a) shows the mean daily 8-hour averaged O₃ concentration (MDA8), a common surface O₃ metric, derived from the simulated hourly O₃ concentration at the lowest model level affecting global vegetation under the Sitch O₃ damage scheme. Global GPP are 133.6 Pg C yr⁻¹ and 131.8 Pg C yr⁻¹ for Sitch O₃ scheme at low and high sensitivity, respectively (Table 5), both of which are smaller than the 134.7 Pg C yr⁻¹ from the simulation without O₃ damage (Figure 7(b)). These global GPP reductions are seemingly small (<1% to ~2%) and conceal larger regional changes. Figure 9(c) shows that the Sitch O₃ damage scheme at high sensitivity leads to an up to 15% reduction in GPP whereas low sensitivity shows modest reductions of about half of those magnitudes. Particularly large O₃-induced damages are in highly populated regions (e.g., eastern US, Europe, central Africa, northern India and East Asia) associated with high anthropogenic emissions (NO_x in particular). Many of these regions also contain arable lands, and thus O₃ exposure can also affect food security (Feng et al., 2008; Avnery et al., 2011b; Emberson et al., 2018; Ainsworth et al., 2020; Tai et al., 2021; Leung et al., 2022; Roberts et al., 2022).

Figure 8(b) shows the statistics of Table 4 per region (Figure 8(a)) for simulations with O₃ damage. The presence of O₃ does not affect the model-observation correlations significantly for any region; when compared to the correlations of TEMIR_MO_off simulation results, correlations from O₃ damaged GPP show small differences. O₃ damage reduces the model overestimation with respect to GOSIF GPP. In particular, for eastern China and Central Africa, implementing O₃ damage reduces the positive model biases as seen in Figure 7. Underestimation is worsened for the regions of Temperate North America and East and South Asia where there is strong O₃ damage (Figure 9).

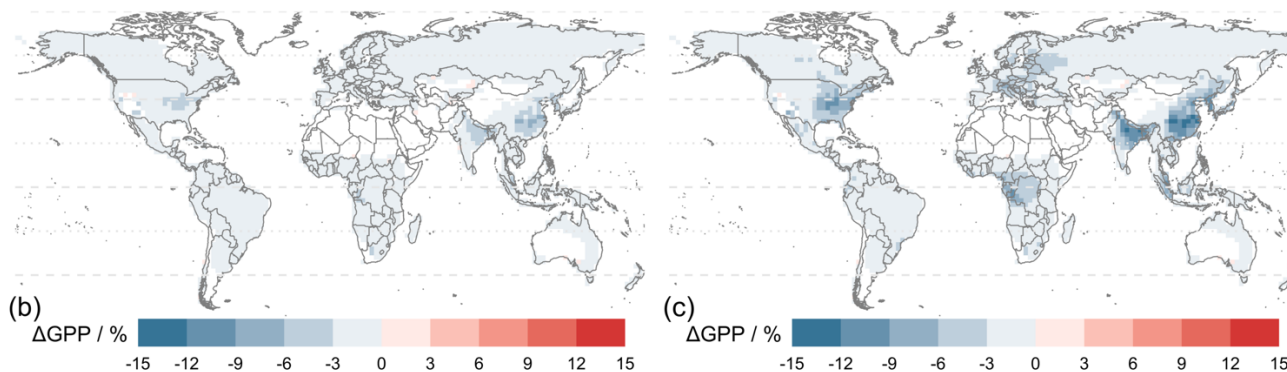
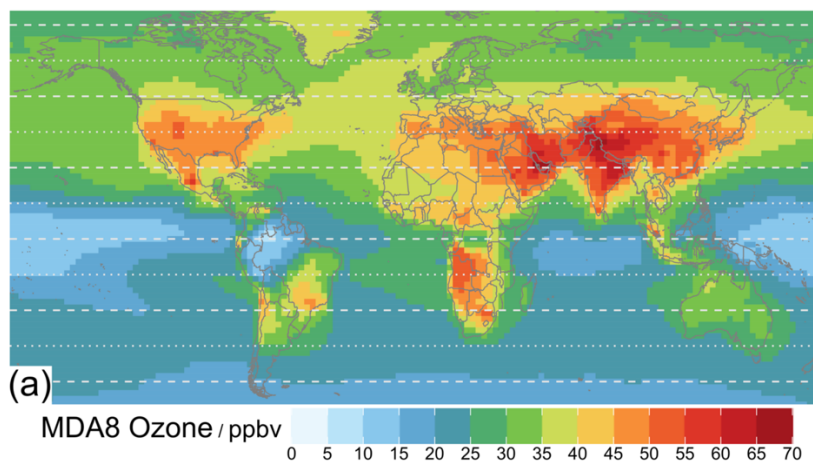


Figure 9: Mean daily 8-hour averaged (MDA8) O₃ concentration of the lowest model layer averaged over years 2010 to 2015; and percentage differences in average global GPP of years 2010 to 2015 of the simulated results with Sitch O₃ damage scheme at (b) low and (c) high sensitivity from the simulation TEMIR_MO_off (Table 2).

5

Figure 10 shows the comparisons between simulations (Table 3) displaying the interplay of CO₂ fertilization effects and O₃ damage on GPP. CO₂ fertilization (from 370 to 390 ppmv), shown in Figure 10(b), promotes regional productivity by up to 7%. Global GPP enhancement is ~2% (Table 5), thus simulations estimate rising atmospheric CO₂ concentration results in global GPP increase of 0.126% ppmv⁻¹. Seen in Figure 10(c), O₃-induced regional reductions are up to 15% under the Sitch O₃ damage scheme at high sensitivity, whereby results are similar to that in Figure 9(c). Figure 10(d) shows the differences in percentage O₃ damage of GPP of the simulation with O₃ damage at a CO₂ concentration of 390 ppmv from that at 370 ppmv (i.e., Fig. 9(c)). The positive values in Fig. 9(d) indicates that the O₃-induced GPP reduction is smaller at a higher CO₂ concentration, reflecting the additional benefits of CO₂ fertilization from the reduced stomatal conductance, which improves water use efficiency and also decreases stomatal O₃ uptake thus lessening O₃-induced impacts.

15

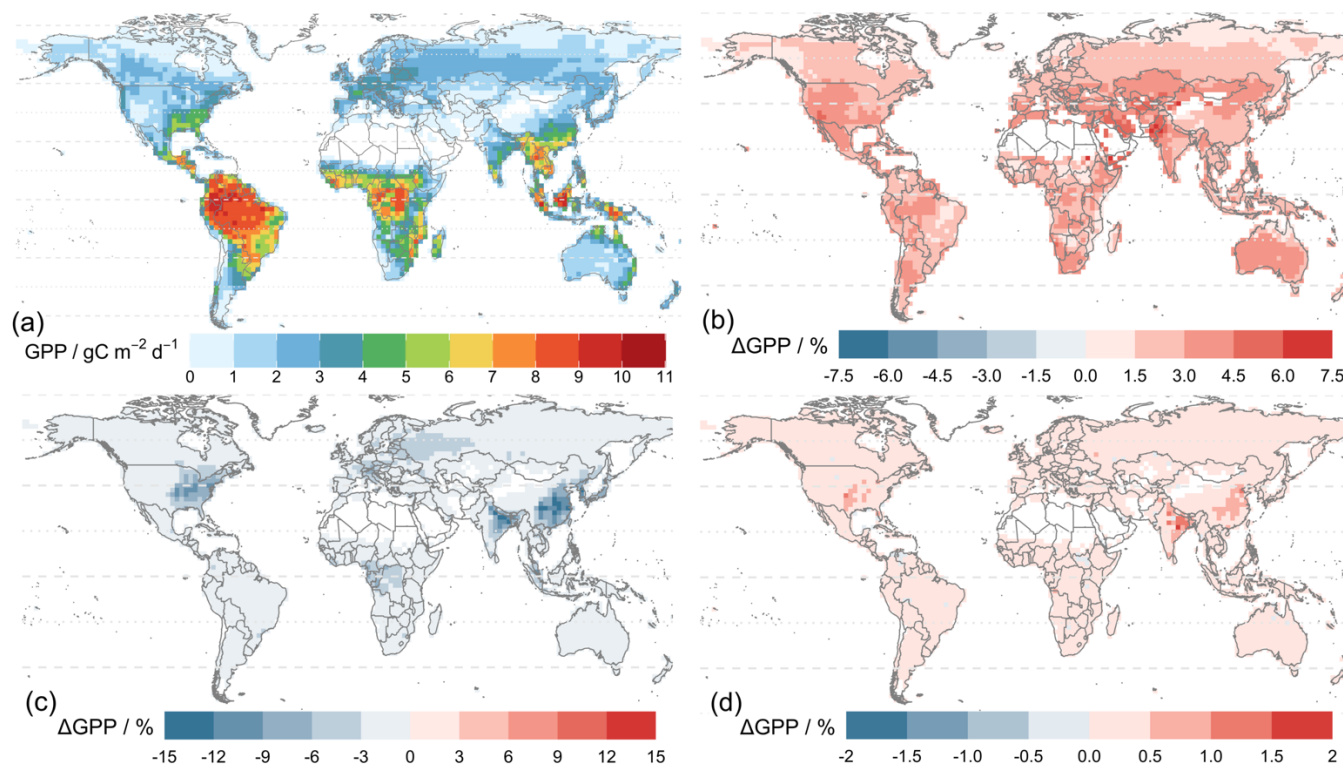


Figure 10: Plots showing results from simulations of Table 3: (a) gross primary product (GPP) modeled for year 2000 at a CO_2 concentration of 370 ppmv (C0_O0), (b) percentage changes in GPP showing CO_2 fertilization effects of year-2010 CO_2 concentration at 390 ppm ($100\% \times (\text{C1_O0} - \text{C0_O0})/\text{C0_O0}$), (c) percentage changes in GPP due to O_3 damage at high sensitivity of the Sitch O_3 damage scheme for year-2000 modeled O_3 concentration and CO_2 concentration of 370 ppmv ($100\% \times (\text{C0_O1} - \text{C0_O0})/\text{C0_O0}$), and (d) differences in percentage O_3 damage at a CO_2 concentration of 390 ppmv from that at 370 ppmv ($100\% \times (\text{C1_O1} - \text{C1_O0})/\text{C1_O0} - 100\% \times (\text{C0_O1} - \text{C0_O0})/\text{C0_O0}$), whereby positive values indicate a reduction in percentage O_3 damage.

6 Discussion and conclusions

In this paper we provide detailed model description of the newly developed Terrestrial Ecosystem Model in R (TEMIR) version 1.0, which simulates ecophysiological processes and functions (most importantly, photosynthesis and GPP) of terrestrial ecosystems as represented by different PFTs, driven by prescribed meteorological conditions and atmospheric chemical composition. We specifically include the multiple parameterization schemes for stomatal O_3 uptake and O_3 damage on plants, and showcase the utility of TEMIR in evaluating the responses of global primary productivity (GPP) to O_3 damage, CO_2 fertilization and their interactions. The productivity simulated at site and global levels reproduces the observed diurnal and seasonal cycles well for evergreen needleleaf and deciduous broadleaf forests (especially those that are mature), with an annual average GPP of $134.7 \text{ Pg C yr}^{-1}$ for years 2010–2015 and a global reduction of up to 2% when O_3 damage is considered. This is validated against the productivity from the 49 FLUXNET sites and GOSIF GPP.



TEMIR-simulated global GPP lies well within the accepted range but the associated large uncertainty is well acknowledged in the field (Bonan et al., 2011; Baldocchi et al., 2016; Zhang et al., 2017; Li and Xiao, 2019; Wild et al., 2021; Bi et al., 2022; Zhang and Ye, 2022), hence limiting the validity of global GPP model-observation comparison in this study (Sect. 5.2). Site-level validation may lend more credence by isolating certain PFTs for comparison, albeit being more limited in scope and scale
5 unlike global comparisons. Our investigation suggests that possible PFT systematic biases exist generally for diurnal productivity, which reflect the limitations of having a set prescribed parameters for generalized classes of plant functions. For instance, there is a systematic underestimation for deciduous broadleaf forests though it can be explained by the uncertainties of LAI datasets (Liu et al., 2018), and some regions show distinctive physiology and phenology of grasses and shrubs. Particularly for semiarid regions where the range of productivity is large, the model shows variable accuracy. Incorporating
10 site-level meteorology in simulations can improve performance for a few selected sites but otherwise comparable to results from simulations with gridded assimilated meteorology as input. This highlights the generalization and coarse resolution that can drastically overlook regional and small-scale nuances. All being said, TEMIR has great skill in capturing annual and seasonal GPP at the global scale and some productive regions and PFTs, whereby correlation is high in the range of 80–90%, showcasing the utility of TEMIR at scales in accordance with the model design. Caution should be taken with good knowledge
15 of model preferences and its underlying theoretical assumptions for any given research question, especially when concerning multifactor land-atmosphere interactions and vegetation responses to various environmental stresses. Further development and validation of the model with detailed observations are crucial to provide more accurate vegetation parametrization for specific applications, e.g., to investigate vegetation responses to droughts and heatwaves composition (e.g., Yan et al., 2022), especially at the regional and site levels. For any specific site, users are recommended to recalibrate relevant model parameters and inputs
20 with site observations, such as LAI, V_{cmax} , PFT, etc., to yield the most accurate results.

The initial motivation and one of the most relevant applications of TEMIR is to address the impacts of O₃ pollution and exposure on terrestrial ecosystem productivity, whereby an active Sitch O₃ damage scheme improves model performance with respect to GPP. Concerning O₃ damage on GPP, there is a good agreement with previous studies in terms of both magnitudes
25 and spatial variations (e.g., Sitch et al., 2007; Lombardozzi et al., 2015). For instance, the OCN model (Franz et al., 2017; Franz and Zaehle, 2021) simulated that O₃ reduces GPP in Europe by ~8% and the JULES land surface model (Slevin et al., 2017) in the range of 10–20% (Oliver et al., 2018). The Yale Interactive terrestrial Biosphere (YIBs) model (Yue and Unger, 2015) simulated that O₃ reduces global GPP by 2–5% with East Asia experiencing damage of 4–10%. Yue and Unger (2014) also showed GPP reductions of 4–8% in the eastern US with high episodes giving a higher range to 11–17%. YIBs has the
30 capability of synchronous coupling (e.g., GEOS-Chem-YIBs; Lei et al., 2020), which reported similar ranges of GPP reductions, globally by 1.5–3.6% and extremes of 11–14% in the eastern US and eastern China. This lends credence to the comparable performance of TEMIR v1.0 that has a more simplistic terrestrial ecosystem with prescribed ecosystem structure (noting that active biogeochemistry is in development). Synchronous model coupling between a CTM or climate model and a fully prognostic biosphere model with active biogeochemistry is particularly suitable for examining O₃-vegetation feedbacks,



especially for timescales long enough (e.g., multidecadal) for ecosystem structure to co-evolve with the atmosphere. For instance, Gong et al. (2021) and Sadiq et al. (2017) showed that dynamic O₃-vegetation interactions can lead to a long-term ecosystem decline and a positive feedback on O₃ concentration in China and worldwide, respectively, worsening air quality. Zhu et al. (2022) found similar positive O₃-vegetation feedbacks in China with the coupled framework using WRF-Chem and Noah-MP. Yue et al. (2017) also investigated O₃-aerosol-vegetation interactions in China. TEMIR can only be asynchronously coupled with GEOS-Chem and is not the best tool for investigating two-way O₃-vegetation interactions, especially when such interactions relevantly happen within a model time step, but it is particularly suitable for estimating first-order effects of O₃ pollution on vegetation in a computationally efficient manner. Zhou et al. (2018) indeed found that second-order effects of O₃ pollution (i.e., additional effects of modified O₃ concentrations after feedbacks are accounted for) on vegetation are negligible. Moreover, asynchronous coupling between TEMIR and GEOS-Chem, for example, and conducting factorial experiments with them can help disentangle complex pathways and feedbacks that are often convoluted in fully coupled models.

We recognize that the O₃ damage scheme in TEMIR does not account for sluggishness in stomatal responses (e.g., Huntingford et al., 2018; Clifton et al., 2020), which may modify further O₃ uptake, although such effect is expected to be small at the resolution relevant for this study. O₃ sensitivities also have crop-related inaccuracies due to the generic crop representation in this version of TEMIR. Such is a common practice in global-scale biosphere models, and Leung et al. (2020) suggested that if a study focuses on crop yields, species-specific calibration is required to reduce uncertainty and likely inaccuracies for the crops concerned. TEMIR v1.0 on a global scale is not suitable for any crop-focused investigations, but one may use the version of TEMIR implemented with additional crop functionalities such as the calculation of phytotoxic ozone dose, taking advantage of the stomatal calculation in TEMIR, and the subsequent estimation of ozone-crop impacts (Tai et al., 2021). The utility of TEMIR in examining vegetation-mediated dry-depositional sinks of O₃ has also been demonstrated (Sun et al., 2022).

Mechanistic representations allow modeling for various meteorological conditions and is invaluable to evaluate ecophysiological responses to a changing climate and intermittent climate extremes (e.g., Bonan, 2008, 2016; Cai and Prentice, 2020; Gang et al., 2022). Ciais et al. (2005) estimated a 30% GPP reduction in Europe following the heatwave in year 2003 and vegetation there became a net carbon source, attributable to the rainfall deficit and extreme summer heat. This was also shown by Bamberger et al. (2017), whereby heat and drought impacts alter photosynthesis and vegetation state. More extreme events are projected for a future climate, which various models (e.g., O-CN, YIBs) have shown to decrease productivity (e.g., Franz and Zaehle, 2021; Yan et al., 2022). He et al. (2022), using models, showed that climate variability is the main factor controlling interannual GPP variability of grasslands in China. Such effect is the most prominent in the summer, which is responsible for more than 40% of decadal GPP variability in Chinese grasslands and the largest in comparison to effects from CO₂ fertilization and nitrogen deposition. Similar to the case for O₃-vegetation coupling discussed above, fully coupled climate-biosphere models can be particularly useful for examining two-way interactions and feedbacks, and also long-term (multi-decadal to multi-centennial) co-evolution of climate and the biosphere. However, the embedded complex interactions



may obscure the relative importance of different factors, making it a lot more difficult to attribute changes to specific factors. Offline modes such as TEMIR are therefore particularly useful for investigating and attributing biospheric variability and changes to prescribed changes in climatic variables.

5 In addition, we have demonstrated the utility of TEMIR in examining the direct and interactive effects of multiple atmospheric chemical species on global vegetation (i.e., CO₂ and O₃ concentrations). CO₂ fertilization in TEMIR results in strong GPP enhancement as seen in many studies (e.g., Schimel et al., 2015; Cai and Prentice, 2020; Chen et al., 2022; Yang et al., 2022). Our simulations estimate that CO₂ fertilization increases global GPP by 0.126% ppmv⁻¹, which is comparable to the value of 0.138% ± 0.007% ppmv⁻¹ reported by Ueyama et al. (2020). It is noteworthy that some studies (e.g., Lee et al., 2018) suggested
10 that overlooking spatiotemporal variability of atmospheric CO₂ can lead to inaccuracies for seasonal and regional GPP estimation but only minor influence on global GPP. Additional crop functionalities of TEMIR (Tai et al., 2021) can also address the CO₂ fertilization effects on crops, although studies have also found that the resulted productivity increase gives larger yield quantity but does not necessarily translate to increased yield quality (Myers et al., 2014; Ebi et al., 2021; Xia et al., 2021). The competing effects of CO₂ fertilization and O₃ damage on vegetation have been well documented in field
15 experiments, although magnitudes vary and are species-dependent (e.g., Oikawa and Ainsworth, 2016; Proietti et al., 2016; Karlsson et al., 2017; Moura et al., 2018; Zhang et al., 2018; Ainsworth et al., 2020; Xia et al., 2021). TEMIR shows that CO₂ fertilization can reduce the percentage O₃ damage on vegetation (~1% globally), which is generally comparable to 1–2% found by Oliver et al. (2018), whereas Sitch et al. (2007) simulated a higher range of 6–9%. We note that while comparisons among models are useful, we must be mindful of the differences in model designs and setups (as mentioned in Sect. 1). Miner et al.
20 (2017) cautioned that stomatal responses to CO₂ can be highly species-dependent and variable under different soil conditions, adding more uncertainty to the parameterization of CO₂-O₃-vegetation interactions. The changing nitrogen deposition due to anthropogenic activities may likewise influence the interactions between vegetation, CO₂ and O₃ (e.g., Zhao et al., 2017; Liu et al., 2021). As atmospheric composition rapidly changes in the next century, these interactive mechanisms should be considered for modelers to more representatively and accurately model the future Earth system (e.g., Bytnerowicz et al., 2007;
25 Pu et al., 2017; Sicard et al., 2017; Franz and Zaehle, 2021; Leung et al., 2022).

All in all, the high adaptability of TEMIR, written in an freely open-source, widely used and easy-to-learn programming language (R Core Team, 2022), is expected to facilitate fruitful contribution to research at various spatiotemporal scales on biosphere-atmosphere interaction. It also provides a readily available tool for policy makers, practitioners and other
30 stakeholders to assess the ecosystem services provided by vegetation in different regions or cities, as well as their sensitivities to future atmospheric changes, possibly enhancing the translational value of ecological and geoscientific research.



7 Code availability

The Terrestrial Ecosystem Model in R (version 1.0) source code is publicly available at the repository: <https://doi.org/10.5281/zenodo.6380828>.

8 Author contribution

- 5 APKT conceived the study. APKT developed the TEMIR model. DHYY developed additional model codes and performed the simulations and analysis. APKT and DHYY prepared the paper. TL developed multilayer soil representation and contributed to relevant sections of the paper.

9 Competing interests

- 10 The authors declare no competing interests.

References

- Ainsworth, E. A., Yendrek, C. R., Sitch, S., Collins, W. J., and Emberson, L. D.: The Effects of Tropospheric Ozone on Net Primary Productivity and Implications for Climate Change, *Annu. Rev. Plant Biol.*, 63, 637–661, <https://doi.org/10.1146/annurev-arplant-042110-103829>, 2012.
- 15 Ainsworth, E. A., Lemonnier, P., and Wedow, J. M.: The influence of rising tropospheric carbon dioxide and ozone on plant productivity, *Plant Biol.*, 22, 5–11, <https://doi.org/10.1111/plb.12973>, 2020.
- Anav, A., Menut, L., Khvorostyanov, D., and Viovy, N.: Impact of tropospheric ozone on the Euro-Mediterranean vegetation, *Glob. Change Biol.*, 17, 2342–2359, <https://doi.org/10.1111/j.1365-2486.2010.02387.x>, 2011.
- 20 Arain, M. A., Xu, B., Brodeur, J. J., Khomik, M., Peichl, M., Beamesderfer, E., Restrepo-Couple, N., and Thorne, R.: Heat and drought impact on carbon exchange in an age-sequence of temperate pine forests, *Ecol. Process.*, 11, 7, <https://doi.org/10.1186/s13717-021-00349-7>, 2022.
- Arneth, A., Harrison, S. P., Zaehle, S., Tsigaridis, K., Menon, S., Bartlein, P. J., Feichter, J., Korhola, A., Kulmala, M., O'Donnell, D., Schurgers, G., Sorvari, S., and Vesala, T.: Terrestrial biogeochemical feedbacks in the climate system, *Nat. Geosci.*, 3, 525–532, <https://doi.org/10.1038/ngeo905>, 2010.
- 25 Arora, V. K., Boer, G. J., Friedlingstein, P., Eby, M., Jones, C. D., Christian, J. R., Bonan, G., Bopp, L., Brovkin, V., Cadule, P., Hajima, T., Ilyina, T., Lindsay, K., Tjiputra, J. F., and Wu, T.: Carbon-Concentration and Carbon–Climate Feedbacks in CMIP5 Earth System Models, *J. Clim.*, 26, 5289–5314, <https://doi.org/10.1175/JCLI-D-12-00494.1>, 2013.
- Avnery, S., Mauzerall, D. L., Liu, J., and Horowitz, L. W.: Global crop yield reductions due to surface ozone exposure: 1. Year 2000 crop production losses and economic damage, *Atmos. Environ.*, 45, 2284–2296, <https://doi.org/10.1016/j.atmosenv.2010.11.045>, 2011a.
- 30

Avnery, S., Mauzerall, D. L., Liu, J., and Horowitz, L. W.: Global crop yield reductions due to surface ozone exposure: 2. Year 2030 potential crop production losses and economic damage under two scenarios of O₃ pollution, *Atmos. Environ.*, 45, 2297–2309, <https://doi.org/10.1016/j.atmosenv.2011.01.002>, 2011b.

5 Baldocchi, D., Ryu, Y., and Keenan, T.: Terrestrial Carbon Cycle Variability, *F1000Research*, 5, 2371, <https://doi.org/10.12688/f1000research.8962.1>, 2016.

Ball, J. T., Woodrow, I. E., and Berry, J. A.: A Model Predicting Stomatal Conductance and its Contribution to the Control of Photosynthesis under Different Environmental Conditions, in: *Progress in Photosynthesis Research*, edited by: Biggins, J., Springer Netherlands, Dordrecht, 221–224, https://doi.org/10.1007/978-94-017-0519-6_48, 1987.

10 Bamberger, I., Ruehr, N. K., Schmitt, M., Gast, A., Wohlfahrt, G., and Arneht, A.: Isoprene emission and photosynthesis during heatwaves and drought in black locust, *Biogeosciences*, 14, 3649–3667, <https://doi.org/10.5194/bg-14-3649-2017>, 2017.

15 Beer, C., Reichstein, M., Tomelleri, E., Ciais, P., Jung, M., Carvalhais, N., Rodenbeck, C., Arain, M. A., Baldocchi, D., Bonan, G. B., Bondeau, A., Cescatti, A., Lasslop, G., Lindroth, A., Lomas, M., Luysaert, S., Margolis, H., Oleson, K. W., Rouspard, O., Veenendaal, E., Viovy, N., Williams, C., Woodward, F. I., and Papale, D.: Terrestrial Gross Carbon Dioxide Uptake: Global Distribution and Covariation with Climate, *Science*, 329, 834–838, <https://doi.org/10.1126/science.1184984>, 2010.

Beringer, J., Hutley, L. B., Tapper, N. J., and Cernusak, L. A.: Savanna fires and their impact on net ecosystem productivity in North Australia, *Glob. Change Biol.*, 13, 990–1004, <https://doi.org/10.1111/j.1365-2486.2007.01334.x>, 2007.

20 Beringer, J., Hutley, L. B., Hacker, J. M., Neininger, B., and Paw U, K. T.: Patterns and processes of carbon, water and energy cycles across northern Australian landscapes: From point to region, *Agric. For. Meteorol.*, 151, 1409–1416, <https://doi.org/10.1016/j.agrformet.2011.05.003>, 2011.

Bey, I., Jacob, D. J., Yantosca, R. M., Logan, J. A., Field, B. D., Fiore, A. M., Li, Q., Liu, H. Y., Mickley, L. J., and Schultz, M. G.: Global modeling of tropospheric chemistry with assimilated meteorology: Model description and evaluation, *J. Geophys. Res. Atmospheres*, 106, 23073–23095, <https://doi.org/10.1029/2001JD000807>, 2001.

25 Bi, W., He, W., Zhou, Y., Ju, W., Liu, Y., Liu, Y., Zhang, X., Wei, X., and Cheng, N.: A global 0.05° dataset for gross primary production of sunlit and shaded vegetation canopies from 1992 to 2020, *Sci. Data*, 9, 213, <https://doi.org/10.1038/s41597-022-01309-2>, 2022.

30 Boike, J., Kattenstroth, B., Abramova, K., Bornemann, N., Chetverova, A., Fedorova, I., Fröb, K., Grigoriev, M., Grüber, M., Kutzbach, L., Langer, M., Minke, M., Muster, S., Piel, K., Pfeiffer, E.-M., Stoof, G., Westermann, S., Wischniewski, K., Wille, C., and Hubberten, H.-W.: Baseline characteristics of climate, permafrost, and land cover from a new permafrost observatory in the Lena River Delta, Siberia (1998–2011), *Biogeosciences*, 10, 2105–2128, <https://doi.org/10.5194/bg-10-2105-2013>, 2013.

Bonan, G. B.: Forests and Climate Change: Forcings, Feedbacks, and the Climate Benefits of Forests, *Science*, 320, 1444–1449, <https://doi.org/10.1126/science.1155121>, 2008.

35 Bonan, G. B.: Forests, Climate, and Public Policy: A 500-Year Interdisciplinary Odyssey, *Annu. Rev. Ecol. Evol. Syst.*, 47, 97–121, <https://doi.org/10.1146/annurev-ecolsys-121415-032359>, 2016.

Bonan, G. B., Levis, S., Kergoat, L., and Oleson, K. W.: Landscapes as patches of plant functional types: An integrating concept for climate and ecosystem models, *Glob. Biogeochem. Cycles*, 16, 5-1-5–23, <https://doi.org/10.1029/2000GB001360>, 2002.



- Bonan, G. B., Lawrence, P. J., Oleson, K. W., Levis, S., Jung, M., Reichstein, M., Lawrence, D. M., and Swenson, S. C.: Improving canopy processes in the Community Land Model version 4 (CLM4) using global flux fields empirically inferred from FLUXNET data, *J. Geophys. Res.*, 116, <https://doi.org/10.1029/2010JG001593>, 2011.
- Bytnerowicz, A., Omasa, K., and Paoletti, E.: Integrated effects of air pollution and climate change on forests: A northern hemisphere perspective, *Environ. Pollut.*, 147, 438–445, <https://doi.org/10.1016/j.envpol.2006.08.028>, 2007.
- von Caemmerer, S. and Farquhar, G. D.: Some relationships between the biochemistry of photosynthesis and the gas exchange of leaves, *Planta*, 153, 376–387, <https://doi.org/10.1007/BF00384257>, 1981.
- Cai, W. and Prentice, I. C.: Recent trends in gross primary production and their drivers: analysis and modelling at flux-site and global scales, *Environ. Res. Lett.*, 15, 124050, <https://doi.org/10.1088/1748-9326/abc64e>, 2020.
- 10 Chen, C., Riley, W. J., Prentice, I. C., and Keenan, T. F.: CO₂ fertilization of terrestrial photosynthesis inferred from site to global scales, *Proc. Natl. Acad. Sci.*, 119, e2115627119, <https://doi.org/10.1073/pnas.2115627119>, 2022.
- Chen, M., Rafique, R., Asrar, G. R., Bond-Lamberty, B., Ciais, P., Zhao, F., Reyer, C. P. O., Ostberg, S., Chang, J., Ito, A., Yang, J., Zeng, N., Kalnay, E., West, T., Leng, G., Francois, L., Munhoven, G., Henrot, A., Tian, H., Pan, S., Nishina, K., Viovy, N., Morfopoulos, C., Betts, R., Schaphoff, S., Steinkamp, J., and Hickler, T.: Regional contribution to variability and trends of global gross primary productivity, *Environ. Res. Lett.*, 12, 105005, <https://doi.org/10.1088/1748-9326/aa8978>, 2017.
- 15 Ciais, Ph., Reichstein, M., Viovy, N., Granier, A., Ogée, J., Allard, V., Aubinet, M., Buchmann, N., Bernhofer, Chr., Carrara, A., Chevallier, F., De Noblet, N., Friend, A. D., Friedlingstein, P., Grünwald, T., Heinesch, B., Keronen, P., Knohl, A., Krinner, G., Loustau, D., Manca, G., Matteucci, G., Miglietta, F., Ourcival, J. M., Papale, D., Pilegaard, K., Rambal, S., Seufert, G., Soussana, J. F., Sanz, M. J., Schulze, E. D., Vesala, T., and Valentini, R.: Europe-wide reduction in primary productivity caused by the heat and drought in 2003, *Nature*, 437, 529–533, <https://doi.org/10.1038/nature03972>, 2005.
- 20 Clifton, O. E., Fiore, A. M., Massman, W. J., Baublitz, C. B., Coyle, M., Emberson, L., Fares, S., Farmer, D. K., Gentine, P., Gerosa, G., Guenther, A. B., Helmig, D., Lombardozzi, D. L., Munger, J. W., Patton, E. G., Pusede, S. E., Schwede, D. B., Silva, S. J., Sörgel, M., Steiner, A. L., and Tai, A. P. K.: Dry Deposition of Ozone Over Land: Processes, Measurement, and Modeling, *Rev. Geophys.*, 58, <https://doi.org/10.1029/2019RG000670>, 2020.
- 25 Cohen, A. J., Brauer, M., Burnett, R., Anderson, H. R., Frostad, J., Estep, K., Balakrishnan, K., Brunekreef, B., Dandona, L., Dandona, R., Feigin, V., Freedman, G., Hubbell, B., Jobling, A., Kan, H., Knibbs, L., Liu, Y., Martin, R., Morawska, L., Pope, C. A., Shin, H., Straif, K., Shaddick, G., Thomas, M., Dingenen, R. van, Donkelaar, A. van, Vos, T., Murray, C. J. L., and Forouzanfar, M. H.: Estimates and 25-year trends of the global burden of disease attributable to ambient air pollution: an analysis of data from the Global Burden of Diseases Study 2015, *The Lancet*, 389, 1907–1918, [https://doi.org/10.1016/S0140-6736\(17\)30505-6](https://doi.org/10.1016/S0140-6736(17)30505-6), 2017.
- 30 Collatz, G., Ribas-Carbo, M., and Berry, J.: Coupled Photosynthesis-Stomatal Conductance Model for Leaves of C₄ Plants, *Funct. Plant Biol.*, 19, <https://doi.org/10.1071/PP9920519>, 1992.
- Collatz, G. J., Ball, J. T., Grivet, C., and Berry, J. A.: Physiological and environmental regulation of stomatal conductance, photosynthesis and transpiration: a model that includes a laminar boundary layer, *Agric. For. Meteorol.*, 54, 107–136, [https://doi.org/10.1016/0168-1923\(91\)90002-8](https://doi.org/10.1016/0168-1923(91)90002-8), 1991.
- 35 Dermody, O., Long, S. P., McConnaughay, K., and DeLucia, E. H.: How do elevated CO₂ and O₃ affect the interception and utilization of radiation by a soybean canopy?, *Glob. Change Biol.*, 14, 556–564, <https://doi.org/10.1111/j.1365-2486.2007.01502.x>, 2008.



- Dickinson, R. E.: Land Surface Processes and Climate—Surface Albedos and Energy Balance, in: *Advances in Geophysics*, vol. 25, Elsevier, 305–353, [https://doi.org/10.1016/S0065-2687\(08\)60176-4](https://doi.org/10.1016/S0065-2687(08)60176-4), 1983.
- Dlugokencky, E. and Tans, P.: Trends in atmospheric carbon dioxide, National Oceanic and Atmospheric Administration, Earth System Research Laboratory (NOAA/ESRL), 2022.
- 5 Dušek, J., Čížková, H., Stellner, S., Czerný, R., and Květ, J.: Fluctuating water table affects gross ecosystem production and gross radiation use efficiency in a sedge-grass marsh, *Hydrobiologia*, 692, 57–66, <https://doi.org/10.1007/s10750-012-0998-z>, 2012.
- Ebi, K. L., Anderson, C. L., Hess, J. J., Kim, S.-H., Loladze, I., Neumann, R. B., Singh, D., Ziska, L., and Wood, R.: Nutritional quality of crops in a high CO₂ world: an agenda for research and technology development, *Environ. Res. Lett.*, 16, 064045, <https://doi.org/10.1088/1748-9326/abfcfa>, 2021.
- 10 Emberson, L. D., Kitwiroon, N., Beevers, S., Büker, P., and Cinderby, S.: Scorched Earth: how will changes in the strength of the vegetation sink to ozone deposition affect human health and ecosystems?, *Atmospheric Chem. Phys.*, 13, 6741–6755, <https://doi.org/10.5194/acp-13-6741-2013>, 2013.
- Emberson, L. D., Pleijel, H., Ainsworth, E. A., van den Berg, M., Ren, W., Osborne, S., Mills, G., Pandey, D., Dentener, F.,
15 Büker, P., Ewert, F., Koeble, R., and Van Dingenen, R.: Ozone effects on crops and consideration in crop models, *Eur. J. Agron.*, 100, 19–34, <https://doi.org/10.1016/j.eja.2018.06.002>, 2018.
- Fares, S., Vargas, R., Detto, M., Goldstein, A. H., Karlik, J., Paoletti, E., and Vitale, M.: Tropospheric ozone reduces carbon assimilation in trees: estimates from analysis of continuous flux measurements, *Glob. Change Biol.*, 19, 2427–2443, <https://doi.org/10.1111/gcb.12222>, 2013.
- 20 Farquhar, G. D., von Caemmerer, S., and Berry, J. A.: A biochemical model of photosynthetic CO₂ assimilation in leaves of C₃ species, *Planta*, 149, 78–90, <https://doi.org/10.1007/BF00386231>, 1980.
- Felzer, B. S., Cronin, T., Reilly, J. M., Melillo, J. M., and Wang, X.: Impacts of ozone on trees and crops, *Comptes Rendus Geosci.*, 339, 784–798, <https://doi.org/10.1016/j.crte.2007.08.008>, 2007.
- Feng, Z., Kobayashi, K., and Ainsworth, E. A.: Impact of elevated ozone concentration on growth, physiology, and yield of wheat (*Triticum aestivum* L.): a meta-analysis, *Glob. Change Biol.*, 14, 2696–2708, <https://doi.org/10.1111/j.1365-2486.2008.01673.x>, 2008.
- 25 Franks, P. J., Adams, M. A., Amthor, J. S., Barbour, M. M., Berry, J. A., Ellsworth, D. S., Farquhar, G. D., Ghannoum, O., Lloyd, J., McDowell, N., Norby, R. J., Tissue, D. T., and von Caemmerer, S.: Sensitivity of plants to changing atmospheric CO₂ concentration: from the geological past to the next century, *New Phytol.*, 197, 1077–1094, <https://doi.org/10.1111/nph.12104>, 2013.
- 30 Franks, P. J., Berry, J. A., Lombardozzi, D. L., and Bonan, G. B.: Stomatal Function across Temporal and Spatial Scales: Deep-Time Trends, Land-Atmosphere Coupling and Global Models, *Plant Physiol.*, 174, 583–602, <https://doi.org/10.1104/pp.17.00287>, 2017.
- Franz, M. and Zaehle, S.: Competing effects of nitrogen deposition and ozone exposure on northern hemispheric terrestrial carbon uptake and storage, 1850–2099, *Biogeosciences*, 18, 3219–3241, <https://doi.org/10.5194/bg-18-3219-2021>, 2021.
- 35 Franz, M., Simpson, D., Arneth, A., and Zaehle, S.: Development and evaluation of an ozone deposition scheme for coupling to a terrestrial biosphere model, *Biogeosciences*, 14, 45–71, <https://doi.org/10.5194/bg-14-45-2017>, 2017.



- Gang, C., Wang, Z., You, Y., Liu, Y., Xu, R., Bian, Z., Pan, N., Gao, X., Chen, M., and Zhang, M.: Divergent responses of terrestrial carbon use efficiency to climate variation from 2000 to 2018, *Glob. Planet. Change*, 208, 103709, <https://doi.org/10.1016/j.gloplacha.2021.103709>, 2022.
- 5 Ganzeveld, L. and Lelieveld, J.: Dry deposition parameterization in a chemistry general circulation model and its influence on the distribution of reactive trace gases, *J. Geophys. Res.*, 100, 20999, <https://doi.org/10.1029/95JD02266>, 1995.
- Ganzeveld, L., Bouwman, L., Stehfest, E., van Vuuren, D. P., Eickhout, B., and Lelieveld, J.: Impact of future land use and land cover changes on atmospheric chemistry-climate interactions, *J. Geophys. Res.*, 115, <https://doi.org/10.1029/2010JD014041>, 2010.
- 10 Gelaro, R., McCarty, W., Suárez, M. J., Todling, R., Molod, A., Takacs, L., Randles, C. A., Darmenov, A., Bosilovich, M. G., Reichle, R., Wargan, K., Coy, L., Cullather, R., Draper, C., Akella, S., Buchard, V., Conaty, A., da Silva, A. M., Gu, W., Kim, G.-K., Koster, R., Lucchesi, R., Merkova, D., Nielsen, J. E., Partyka, G., Pawson, S., Putman, W., Rienecker, M., Schubert, S. D., Sienkiewicz, M., and Zhao, B.: The Modern-Era Retrospective Analysis for Research and Applications, Version 2 (MERRA-2), *J. Clim.*, 30, 5419–5454, <https://doi.org/10.1175/JCLI-D-16-0758.1>, 2017.
- 15 Gong, C., Liao, H., Yue, X., Ma, Y., and Lei, Y.: Impacts of Ozone-Vegetation Interactions on Ozone Pollution Episodes in North China and the Yangtze River Delta, *Geophys. Res. Lett.*, 48, <https://doi.org/10.1029/2021GL093814>, 2021.
- Guenther, A. B., Jiang, X., Heald, C. L., Sakulyanontvittaya, T., Duhl, T., Emmons, L. K., and Wang, X.: The Model of Emissions of Gases and Aerosols from Nature version 2.1 (MEGAN2.1): an extended and updated framework for modeling biogenic emissions, *Geosci. Model Dev.*, 5, 1471–1492, <https://doi.org/10.5194/gmd-5-1471-2012>, 2012.
- 20 Halladay, K. and Good, P.: Non-linear interactions between CO₂ radiative and physiological effects on Amazonian evapotranspiration in an Earth system model, *Clim. Dyn.*, 49, 2471–2490, <https://doi.org/10.1007/s00382-016-3449-0>, 2017.
- Hardacre, C., Wild, O., and Emberson, L.: An evaluation of ozone dry deposition in global scale chemistry climate models, *Atmospheric Chem. Phys.*, 15, 6419–6436, <https://doi.org/10.5194/acp-15-6419-2015>, 2015.
- 25 Haverd, V., Raupach, M. R., Briggs, P. R., Canadell, J. G., Isaac, P., Pickett-Heaps, C., Roxburgh, S. H., van Gorsel, E., Viscarra Rossel, R. A., and Wang, Z.: Multiple observation types reduce uncertainty in Australia’s terrestrial carbon and water cycles, *Biogeosciences*, 10, 2011–2040, <https://doi.org/10.5194/bg-10-2011-2013>, 2013.
- He, P., Ma, X., and Sun, Z.: Interannual variability in summer climate change controls GPP long-term changes, *Environ. Res.*, 212, 113409, <https://doi.org/10.1016/j.envres.2022.113409>, 2022.
- 30 Hoesly, R. M., Smith, S. J., Feng, L., Klimont, Z., Janssens-Maenhout, G., Pitkanen, T., Seibert, J. J., Vu, L., Andres, R. J., Bolt, R. M., Bond, T. C., Dawidowski, L., Kholod, N., Kurokawa, J., Li, M., Liu, L., Lu, Z., Moura, M. C. P., O’Rourke, P. R., and Zhang, Q.: Historical (1750–2014) anthropogenic emissions of reactive gases and aerosols from the Community Emissions Data System (CEDS), *Geosci. Model Dev.*, 11, 369–408, <https://doi.org/10.5194/gmd-11-369-2018>, 2018.
- 35 Hu, L., Keller, C. A., Long, M. S., Sherwen, T., Auer, B., Da Silva, A., Nielsen, J. E., Pawson, S., Thompson, M. A., Trayanov, A. L., Travis, K. R., Grange, S. K., Evans, M. J., and Jacob, D. J.: Global simulation of tropospheric chemistry at 12.5km resolution: performance and evaluation of the GEOS-Chem chemical module (v10-1) within the NASA GEOS Earth System Model (GEOS-5 ESM), *Geosci. Model Dev. Discuss.*, 1–32, <https://doi.org/10.5194/gmd-2018-111>, 2018.
- Huntingford, C., Oliver, R. J., Mercado, L. M., and Sitch, S.: Technical Note: A simple theoretical model framework to describe plant stomatal “sluggishness” in response to elevated ozone concentrations, *Biogeosciences*, 5415–5422, <https://doi.org/10.5194/bg-15-5415-2018>, 2018.



- Hutley, L. B., Beringer, J., Isaac, P. R., Hacker, J. M., and Cernusak, L. A.: A sub-continental scale living laboratory: Spatial patterns of savanna vegetation over a rainfall gradient in northern Australia, *Agric. For. Meteorol.*, 151, 1417–1428, <https://doi.org/10.1016/j.agrformet.2011.03.002>, 2011.
- 5 Im, U., Brandt, J., Geels, C., Hansen, K. M., Christensen, J. H., Andersen, M. S., Solazzo, E., Kioutsioukis, I., Alyuz, U., Balzarini, A., Baro, R., Bellasio, R., Bianconi, R., Bieser, J., Colette, A., Curci, G., Farrow, A., Flemming, J., Fraser, A., Jimenez-Guerrero, P., Kitwiroon, N., Liang, C.-K., Nopmongcol, U., Pirovano, G., Pozzoli, L., Prank, M., Rose, R., Sokhi, R., Tuccella, P., Unal, A., Vivanco, M. G., West, J., Yarwood, G., Hogrefe, C., and Galmarini, S.: Assessment and economic valuation of air pollution impacts on human health over Europe and the United States as calculated by a multi-model ensemble in the framework of AQMEII3, *Atmospheric Chem. Phys.*, 18, 5967–5989, <https://doi.org/10.5194/acp-18-5967-2018>, 2018.
- 10 Imer, D., Merbold, L., Eugster, W., and Buchmann, N.: Temporal and spatial variations of soil CO₂, CH₄ and N₂O fluxes at three differently managed grasslands, *Biogeosciences*, 10, 5931–5945, <https://doi.org/10.5194/bg-10-5931-2013>, 2013.
- Jian, J., Bailey, V., Dorheim, K., Konings, A. G., Hao, D., Shiklomanov, A. N., Snyder, A., Steele, M., Teramoto, M., Vargas, R., and Bond-Lamberty, B.: Historically inconsistent productivity and respiration fluxes in the global terrestrial carbon cycle, *Nat. Commun.*, 13, 1733, <https://doi.org/10.1038/s41467-022-29391-5>, 2022.
- 15 Karlsson, P. E., Uddling, J., Braun, S., Broadmeadow, M., Elvira, S., Gimeno, B. S., Le Thiec, D., Oksanen, E., Vandermeiren, K., Wilkinson, M., and Emberson, L.: New critical levels for ozone effects on young trees based on AOT40 and simulated cumulative leaf uptake of ozone, *Atmos. Environ.*, 38, 2283–2294, <https://doi.org/10.1016/j.atmosenv.2004.01.027>, 2004.
- Karlsson, P. E., Klingberg, J., Engardt, M., Andersson, C., Langner, J., Karlsson, G. P., and Pleijel, H.: Past, present and future concentrations of ground-level ozone and potential impacts on ecosystems and human health in northern Europe, *Sci. Total Environ.*, 576, 22–35, <https://doi.org/10.1016/j.scitotenv.2016.10.061>, 2017.
- 20 Keller, C. A., Long, M. S., Yantosca, R. M., Da Silva, A. M., Pawson, S., and Jacob, D. J.: HEMCO v1.0: a versatile, ESMF-compliant component for calculating emissions in atmospheric models, *Geosci. Model Dev.*, 7, 1409–1417, <https://doi.org/10.5194/gmd-7-1409-2014>, 2014.
- Lai, J., Lortie, C. J., Muenchen, R. A., Yang, J., and Ma, K.: Evaluating the popularity of R in ecology, *Ecosphere*, 10, <https://doi.org/10.1002/ecs2.2567>, 2019.
- 25 Lam, J. C. Y., Tai, A. P. K., Ducker, J. A., and Holmes, C. D.: Development of an ecophysiology module in the GEOS-Chem chemical transport model version 12.2.0 to represent biosphere–atmosphere fluxes relevant for ozone air quality, *Geosci. Model Dev.*, 16, 2323–2342, <https://doi.org/10.5194/gmd-16-2323-2023>, 2023.
- Lasslop, G., Reichstein, M., Papale, D., Richardson, A. D., Arneth, A., Barr, A., Stoy, P., and Wohlfahrt, G.: Separation of net ecosystem exchange into assimilation and respiration using a light response curve approach: critical issues and global evaluation, *Glob. Change Biol.*, 16, 187–208, <https://doi.org/10.1111/j.1365-2486.2009.02041.x>, 2010.
- 30 Lawrence, D., Rosie Fisher, Charles Koven, Keith Oleson, Sean Swenson, Mariana Vertenstein, Ben Andre, Gordon Bonan, Bardan Ghimire, Leo van Kampenhout, Daniel Kennedy, Erik Kluzek, Ryan Knox, Peter Lawrence, Fang Li, Hongyi Li, Danica Lombardozi, Yaqiong Lu, Justin Perket, William Riley, William Sacks, Mingjie Shi, Will Wieder, Chonggang Xu, Ashehad Ali, Andrew Badger, Gautam Bisht, Patrick Broxton, Michael Brunke, Jonathan Buzan, Martyn Clark, Tony Craig, Kyla Dahlin, Beth Drewniak, Louisa Emmons, Josh Fisher, Mark Flanner, Pierre Gentine, Jan Lenaerts, Sam Levis, L. Ruby Leung, William Lipscomb, Jon Pelletier, Daniel M. Ricciuto, Ben Sanderson, Jacquelyn Shuman, Andrew Slater, Zachary Subin, Jinyun Tang, Ahmed Tawfik, Quinn Thomas, Simone Tilmes, Francis Vitt, and Xubin Zeng: Technical Description of version 5.0 of the Community Land Model (CLM), 350, 2020.



- Lawrence, P. J. and Chase, T. N.: Representing a new MODIS consistent land surface in the Community Land Model (CLM 3.0), *J. Geophys. Res.*, 112, G01023, <https://doi.org/10.1029/2006JG000168>, 2007.
- Le Quéré, C., Moriarty, R., Andrew, R. M., Canadell, J. G., Sitch, S., Korsbakken, J. I., Friedlingstein, P., Peters, G. P., Andres, R. J., Boden, T. A., Houghton, R. A., House, J. I., Keeling, R. F., Tans, P., Arneeth, A., Bakker, D. C. E., Barbero, L., Bopp, L., Chang, J., Chevallier, F., Chini, L. P., Ciais, P., Fader, M., Feely, R. A., Gkritzalis, T., Harris, I., Hauck, J., Ilyina, T., Jain, A. K., Kato, E., Kitidis, V., Klein Goldewijk, K., Koven, C., Landschützer, P., Lauvset, S. K., Lefèvre, N., Lenton, A., Lima, I. D., Metzl, N., Millero, F., Munro, D. R., Murata, A., Nabel, J. E. M. S., Nakaoka, S., Nojiri, Y., O'Brien, K., Olsen, A., Ono, T., Pérez, F. F., Pfeil, B., Pierrot, D., Poulter, B., Rehder, G., Rödenbeck, C., Saito, S., Schuster, U., Schwinger, J., Séférian, R., Steinhoff, T., Stocker, B. D., Sutton, A. J., Takahashi, T., Tilbrook, B., van der Laan-Luijkx, I. T., van der Werf, G. R., van Heuven, S., Vandemark, D., Viovy, N., Wiltshire, A., Zaehe, S., and Zeng, N.: Global Carbon Budget 2015, *Earth Syst. Sci. Data*, 7, 349–396, <https://doi.org/10.5194/essd-7-349-2015>, 2015.
- Lee, E., Zeng, F.-W., Koster, R. D., Weir, B., Ott, L. E., and Poulter, B.: The impact of spatiotemporal variability in atmospheric CO₂ concentration on global terrestrial carbon fluxes, *Biogeosciences*, 15, 5635–5652, <https://doi.org/10.5194/bg-15-5635-2018>, 2018.
- Legates, D. R. and McCabe, G. J.: Evaluating the use of “goodness-of-fit” Measures in hydrologic and hydroclimatic model validation, *Water Resour. Res.*, 35, 233–241, <https://doi.org/10.1029/1998WR900018>, 1999.
- Lei, Y., Yue, X., Liao, H., Gong, C., and Zhang, L.: Implementation of Yale Interactive terrestrial Biosphere model v1.0 into GEOS-Chem v12.0.0: a tool for biosphere–chemistry interactions, *Geosci. Model Dev.*, 13, 1137–1153, <https://doi.org/10.5194/gmd-13-1137-2020>, 2020.
- Leung, F., Williams, K., Sitch, S., Tai, A. P. K., Wiltshire, A., Gornall, J., Ainsworth, E. A., Arkebauer, T., and Scoby, D.: Calibrating soybean parameters in JULES 5.0 from the US-Ne2/3 FLUXNET sites and the SoyFACE-O₃ experiment, *Geosci. Model Dev.*, 13, 6201–6213, <https://doi.org/10.5194/gmd-13-6201-2020>, 2020.
- Leung, F., Sitch, S., Tai, A. P. K., Wiltshire, A. J., Gornall, J. L., Folberth, G. A., and Unger, N.: CO₂ fertilization of crops offsets yield losses due to future surface ozone damage and climate change, *Environ. Res. Lett.*, 17, 074007, <https://doi.org/10.1088/1748-9326/ac7246>, 2022.
- Li and Xiao: Mapping Photosynthesis Solely from Solar-Induced Chlorophyll Fluorescence: A Global, Fine-Resolution Dataset of Gross Primary Production Derived from OCO-2, *Remote Sens.*, 11, 2563, <https://doi.org/10.3390/rs11212563>, 2019.
- Li, J., Mahalov, A., and Hyde, P.: Simulating the impacts of chronic ozone exposure on plant conductance and photosynthesis, and on the regional hydroclimate using WRF/Chem, *Environ. Res. Lett.*, 11, 114017, <https://doi.org/10.1088/1748-9326/11/11/114017>, 2016.
- Li, X., Xiao, J., He, B., Altaf Arain, M., Beringer, J., Desai, A. R., Emmel, C., Hollinger, D. Y., Krasnova, A., Mammarella, I., Noe, S. M., Ortiz, P. S., Rey-Sanchez, A. C., Rocha, A. V., and Varlagin, A.: Solar-induced chlorophyll fluorescence is strongly correlated with terrestrial photosynthesis for a wide variety of biomes: First global analysis based on OCO-2 and flux tower observations, *Glob. Change Biol.*, 24, 3990–4008, <https://doi.org/10.1111/gcb.14297>, 2018.
- Lin, H., Jacob, D. J., Lundgren, E. W., Sulprizio, M. P., Keller, C. A., Fritz, T. M., Eastham, S. D., Emmons, L. K., Campbell, P. C., Baker, B., Saylor, R. D., and Montuoro, R.: Harmonized Emissions Component (HEMCO) 3.0 as a versatile emissions component for atmospheric models: application in the GEOS-Chem, NASA GEOS, WRF-GC, CESM2, NOAA GEFS-Aerosol, and NOAA UFS models, *Geosci. Model Dev.*, 14, 5487–5506, <https://doi.org/10.5194/gmd-14-5487-2021>, 2021.



- Lindauer, M., Schmid, H. P., Grote, R., Mauder, M., Steinbrecher, R., and Wolpert, B.: Net ecosystem exchange over a non-cleared wind-throw-disturbed upland spruce forest—Measurements and simulations, *Agric. For. Meteorol.*, 197, 219–234, <https://doi.org/10.1016/j.agrformet.2014.07.005>, 2014.
- 5 Liu, X., Tai, A. P. K., and Fung, K. M.: Responses of surface ozone to future agricultural ammonia emissions and subsequent nitrogen deposition through terrestrial ecosystem changes, *Atmospheric Chem. Phys.*, 21, 17743–17758, <https://doi.org/10.5194/acp-21-17743-2021>, 2021.
- Liu, Y., Xiao, J., Ju, W., Zhu, G., Wu, X., Fan, W., Li, D., and Zhou, Y.: Satellite-derived LAI products exhibit large discrepancies and can lead to substantial uncertainty in simulated carbon and water fluxes, *Remote Sens. Environ.*, 206, 174–188, <https://doi.org/10.1016/j.rse.2017.12.024>, 2018.
- 10 Lombardozzi, D., Levis, S., Bonan, G., and Sparks, J. P.: Predicting photosynthesis and transpiration responses to ozone: decoupling modeled photosynthesis and stomatal conductance, *Biogeosciences*, 9, 3113–3130, <https://doi.org/10.5194/bg-9-3113-2012>, 2012.
- Lombardozzi, D., Levis, S., Bonan, G., Hess, P. G., and Sparks, J. P.: The Influence of Chronic Ozone Exposure on Global Carbon and Water Cycles, *J. Clim.*, 28, 292–305, <https://doi.org/10.1175/JCLI-D-14-00223.1>, 2015.
- 15 Loveland, T. R. and Belward, A. S.: The IGBP-DIS global 1km land cover data set, DISCover: First results, *Int. J. Remote Sens.*, 18, 3289–3295, <https://doi.org/10.1080/014311697217099>, 1997.
- Marcolla, B., Cescatti, A., Manca, G., Zorer, R., Cavagna, M., Fiora, A., Gianelle, D., Rodeghiero, M., Sottocornola, M., and Zampedri, R.: Climatic controls and ecosystem responses drive the inter-annual variability of the net ecosystem exchange of an alpine meadow, *Agric. For. Meteorol.*, 151, 1233–1243, <https://doi.org/10.1016/j.agrformet.2011.04.015>, 2011.
- 20 McLaughlin, S. B., Wullschleger, S. D., Sun, G., and Nosal, M.: Interactive effects of ozone and climate on water use, soil moisture content and streamflow in a southern Appalachian forest in the USA, *New Phytol.*, 174, 125–136, <https://doi.org/10.1111/j.1469-8137.2007.01970.x>, 2007.
- Medlyn, B. E., Duursma, R. A., Eamus, D., Ellsworth, D. S., Prentice, I. C., Barton, C. V. M., Crous, K. Y., De Angelis, P., Freeman, M., and Wingate, L.: Reconciling the optimal and empirical approaches to modelling stomatal conductance, *Glob. Change Biol.*, 17, 2134–2144, <https://doi.org/10.1111/j.1365-2486.2010.02375.x>, 2011.
- 25 Miner, G. L., Bauerle, W. L., and Baldocchi, D. D.: Estimating the sensitivity of stomatal conductance to photosynthesis: a review: The sensitivity of conductance to photosynthesis, *Plant Cell Environ.*, 40, 1214–1238, <https://doi.org/10.1111/pce.12871>, 2017.
- Monin, A. S. and Obukhov, A. M.: Basic laws of turbulent mixing in the surface layer of the atmosphere, *Akad. Nauk Sssr Inst. Geofiz.*, 24, 163–187, 1954.
- 30 Monks, P. S., Archibald, A. T., Colette, A., Cooper, O., Coyle, M., Derwent, R., Fowler, D., Granier, C., Law, K. S., Mills, G. E., Stevenson, D. S., Tarasova, O., Thouret, V., von Schneidemesser, E., Sommariva, R., Wild, O., and Williams, M. L.: Tropospheric ozone and its precursors from the urban to the global scale from air quality to short-lived climate forcer, *Atmospheric Chem. Phys.*, 15, 8889–8973, <https://doi.org/10.5194/acp-15-8889-2015>, 2015.
- 35 Moura, B. B., Alves, E. S., Marabesi, M. A., de Souza, S. R., Schaub, M., and Vollenweider, P.: Ozone affects leaf physiology and causes injury to foliage of native tree species from the tropical Atlantic Forest of southern Brazil, *Sci. Total Environ.*, 610–611, 912–925, <https://doi.org/10.1016/j.scitotenv.2017.08.130>, 2018.



- Myers, S. S., Zanobetti, A., Kloog, I., Huybers, P., Leakey, A. D. B., Bloom, A. J., Carlisle, E., Dietterich, L. H., Fitzgerald, G., Hasegawa, T., Holbrook, N. M., Nelson, R. L., Ottman, M. J., Raboy, V., Sakai, H., Sartor, K. A., Schwartz, J., Seneweera, S., Tausz, M., and Usui, Y.: Increasing CO₂ threatens human nutrition, *Nature*, 510, 139–142, <https://doi.org/10.1038/nature13179>, 2014.
- 5 Noormets, A., Kull, O., Söber, A., Kubiske, M. E., and Karnosky, D. F.: Elevated CO₂ response of photosynthesis depends on ozone concentration in aspen, *Environ. Pollut.*, 158, 992–999, <https://doi.org/10.1016/j.envpol.2009.10.009>, 2010.
- Norman, J. M.: Simulation of microclimates, in: *Biometeorology and Integrated Pest Management*, Academic Press, New York, 65–99, 1982.
- Nowak, D., Hirabayashi, S., Bodine, A., and Greenfield, E.: Tree and forest effects on air quality and human health in the
10 United States, USDA For. Serv. UNL Fac. Publ., 2014.
- Oikawa, S. and Ainsworth, E. A.: Changes in leaf area, nitrogen content and canopy photosynthesis in soybean exposed to an ozone concentration gradient, *Environ. Pollut.*, 215, 347–355, <https://doi.org/10.1016/j.envpol.2016.05.005>, 2016.
- Oleson, K. W. and Lawrence, D. M.: Technical Description of version 4.5 of the Community Land Model (CLM), 434, 2013.
- Oleson, K. W., Lawrence, D. M., Bonan, G. B., Drewniak, B., Huang, M., Levis, S., Li, F., Riley, W. J., Swenson, S. C.,
15 Thornton, P. E., Bozbiyik, A., Fisher, R., Heald, C. L., Kluzek, E., Lamarque, F., Lawrence, P. J., Leung, L. R., Muszala, S., Ricciuto, D. M., Sacks, W., Sun, Y., Tang, J., and Yang, Z.-L.: Technical Description of version 4.5 of the Community Land Model (CLM), 434, 2013.
- Oliver, R. J., Mercado, L. M., Sitch, S., Simpson, D., Medlyn, B. E., Lin, Y.-S., and Folberth, G. A.: Large but decreasing effect of ozone on the European carbon sink, *Biogeosciences*, 15, 4245–4269, <https://doi.org/10.5194/bg-15-4245-2018>, 2018.
- 20 Pacifico, F., Harrison, S. P., Jones, C. D., Arneth, A., Sitch, S., Weedon, G. P., Barkley, M. P., Palmer, P. I., Serça, D., Potosnak, M., Fu, T.-M., Goldstein, A., Bai, J., and Schurgers, G.: Evaluation of a photosynthesis-based biogenic isoprene emission scheme in JULES and simulation of isoprene emissions under present-day climate conditions, *Atmospheric Chem. Phys.*, 11, 4371–4389, <https://doi.org/10.5194/acp-11-4371-2011>, 2011.
- Pacifico, F., Folberth, G. A., Jones, C. D., Harrison, S. P., and Collins, W. J.: Sensitivity of biogenic isoprene emissions to
25 past, present, and future environmental conditions and implications for atmospheric chemistry, *J. Geophys. Res. Atmospheres*, 117, <https://doi.org/10.1029/2012JD018276>, 2012.
- Parrington, M., Jones, D. B. A., Bowman, K. W., Horowitz, L. W., Thompson, A. M., Tarasick, D. W., and Witte, J. C.: Estimating the summertime tropospheric ozone distribution over North America through assimilation of observations from the Tropospheric Emission Spectrometer, *J. Geophys. Res.*, 113, <https://doi.org/10.1029/2007JD009341>, 2008.
- 30 Peichl, M., Brodeur, J. J., Khomik, M., and Arain, M. A.: Biometric and eddy-covariance based estimates of carbon fluxes in an age-sequence of temperate pine forests, *Agric. For. Meteorol.*, 150, 952–965, <https://doi.org/10.1016/j.agrformet.2010.03.002>, 2010.
- Pleijel, H., Danielsson, H., Ojanperä, K., Temmerman, L. D., Högy, P., Badiani, M., and Karlsson, P. E.: Relationships between ozone exposure and yield loss in European wheat and potato—a comparison of concentration- and flux-based exposure indices,
35 *Atmos. Environ.*, 38, 2259–2269, <https://doi.org/10.1016/j.atmosenv.2003.09.076>, 2004.
- Pongratz, J., Reick, C. H., Raddatz, T., and Claussen, M.: Effects of anthropogenic land cover change on the carbon cycle of the last millennium, *Glob. Biogeochem. Cycles*, 23, GB4001, <https://doi.org/10.1029/2009GB003488>, 2009.



- Pongratz, J., Reick, C. H., Raddatz, T., and Claussen, M.: Biogeophysical versus biogeochemical climate response to historical anthropogenic land cover change, *Geophys. Res. Lett.*, 37, <https://doi.org/10.1029/2010GL043010>, 2010.
- Porporato, A., Laio, F., Ridol, L., and Rodriguez-Iturbe, I.: Plants in water-controlled ecosystems: active role in hydrologic processes and response to water stress III. Vegetation water stress, *Adv. Water Resour.*, 20, 2001.
- 5 Prescher, A.-K., Grünwald, T., and Bernhofer, C.: Land use regulates carbon budgets in eastern Germany: From NEE to NBP, *Agric. For. Meteorol.*, 150, 1016–1025, <https://doi.org/10.1016/j.agrformet.2010.03.008>, 2010.
- Proietti, C., Anav, A., De Marco, A., Sicard, P., and Vitale, M.: A multi-sites analysis on the ozone effects on Gross Primary Production of European forests, *Sci. Total Environ.*, 556, 1–11, <https://doi.org/10.1016/j.scitotenv.2016.02.187>, 2016.
- 10 Pu, X., Wang, T. J., Huang, X., Melas, D., Zanis, P., Papanastasiou, D. K., and Poupkou, A.: Enhanced surface ozone during the heat wave of 2013 in Yangtze River Delta region, China, *Sci. Total Environ.*, 603–604, 807–816, <https://doi.org/10.1016/j.scitotenv.2017.03.056>, 2017.
- R Core Team: R: A language and environment for statistical computing, 2022.
- Reichstein, M., Falge, E., Baldocchi, D., Papale, D., Aubinet, M., Berbigier, P., Bernhofer, C., Buchmann, N., Gilmanov, T., Granier, A., Grunwald, T., Havrankova, K., Ilvesniemi, H., Janous, D., Knohl, A., Laurila, T., Lohila, A., Loustau, D., 15 Matteucci, G., Meyers, T., Miglietta, F., Ourcival, J.-M., Pumpanen, J., Rambal, S., Rotenberg, E., Sanz, M., Tenhunen, J., Seufert, G., Vaccari, F., Vesala, T., Yakir, D., and Valentini, R.: On the separation of net ecosystem exchange into assimilation and ecosystem respiration: review and improved algorithm, *Glob. Change Biol.*, 11, 1424–1439, <https://doi.org/10.1111/j.1365-2486.2005.001002.x>, 2005.
- 20 Rhea, L., King, J., Kubiske, M., Saliendra, N., and Teclaw, R.: Effects of elevated atmospheric CO₂ and tropospheric O₃ on tree branch growth and implications for hydrologic budgeting, *Environ. Pollut.*, 158, 1079–1087, <https://doi.org/10.1016/j.envpol.2009.08.038>, 2010.
- Roberts, H. R., Dodd, I. C., Hayes, F., and Ashworth, K.: Chronic tropospheric ozone exposure reduces seed yield and quality in spring and winter oilseed rape, *Agric. For. Meteorol.*, 316, 108859, <https://doi.org/10.1016/j.agrformet.2022.108859>, 2022.
- 25 Sadiq, M., Tai, A. P. K., Lombardozi, D., and Val Martin, M.: Effects of ozone–vegetation coupling on surface ozone air quality via biogeochemical and meteorological feedbacks, *Atmospheric Chem. Phys.*, 17, 3055–3066, <https://doi.org/10.5194/acp-17-3055-2017>, 2017.
- Sanderson, M. G., Collins, W. J., Hemming, D. L., and Betts, R. A.: Stomatal conductance changes due to increasing carbon dioxide levels: Projected impact on surface ozone levels, *Tellus B Chem. Phys. Meteorol.*, 59, 404–411, <https://doi.org/10.1111/j.1600-0889.2007.00277.x>, 2007.
- 30 Schimel, D., Stephens, B. B., and Fisher, J. B.: Effect of increasing CO₂ on the terrestrial carbon cycle, *Proc. Natl. Acad. Sci.*, 112, 436–441, <https://doi.org/10.1073/pnas.1407302112>, 2015.
- Scott, R. L., Biederman, J. A., Hamerlynck, E. P., and Barron-Gafford, G. A.: The carbon balance pivot point of southwestern U.S. semiarid ecosystems: Insights from the 21st century drought, *J. Geophys. Res. Biogeosciences*, 120, 2612–2624, <https://doi.org/10.1002/2015JG003181>, 2015.
- 35 Sellers, P. J.: Canopy reflectance, photosynthesis and transpiration, *Int. J. Remote Sens.*, 6, 1335–1372, <https://doi.org/10.1080/01431168508948283>, 1985.



- Serrano-Ortiz, P., Domingo, F., Cazorla, A., Were, A., Cuezva, S., Villagarcía, L., Alados-Arboledas, L., and Kowalski, A. S.: Interannual CO₂ exchange of a sparse Mediterranean shrubland on a carbonaceous substrate, *J. Geophys. Res.*, 114, G04015, <https://doi.org/10.1029/2009JG000983>, 2009.
- 5 Shekhar, A., Buchmann, N., and Gharun, M.: How well do recently reconstructed solar-induced fluorescence datasets model gross primary productivity?, *Remote Sens. Environ.*, 283, 113282, <https://doi.org/10.1016/j.rse.2022.113282>, 2022.
- Sicard, P., Anav, A., De Marco, A., and Paoletti, E.: Projected global ground-level ozone impacts on vegetation under different emission and climate scenarios, *Atmospheric Chem. Phys.*, 17, 12177–12196, <https://doi.org/10.5194/acp-17-12177-2017>, 2017.
- 10 Sitch, S., Cox, P. M., Collins, W. J., and Huntingford, C.: Indirect radiative forcing of climate change through ozone effects on the land-carbon sink, *Nature*, 448, 791–794, <https://doi.org/10.1038/nature06059>, 2007.
- Slevin, D., Tett, S. F. B., Exbrayat, J.-F., Bloom, A. A., and Williams, M.: Global evaluation of gross primary productivity in the JULES land surface model v3.4.1, *Geosci. Model Dev.*, 10, 2651–2670, <https://doi.org/10.5194/gmd-10-2651-2017>, 2017.
- 15 Sun, G., McLaughlin, S. B., Porter, J. H., Uddling, J., Mulholland, P. J., Adams, M. B., and Pederson, N.: Interactive influences of ozone and climate on streamflow of forested watersheds, *Glob. Change Biol.*, 18, 3395–3409, <https://doi.org/10.1111/j.1365-2486.2012.02787.x>, 2012.
- Sun, S., Tai, A. P. K., Yung, D. H. Y., Wong, A. Y. H., Ducker, J. A., and Holmes, C. D.: Influence of plant ecophysiology on ozone dry deposition: comparing between multiplicative and photosynthesis-based dry deposition schemes and their responses to rising CO₂ level, *Biogeosciences*, 19, 1753–1776, <https://doi.org/10.5194/bg-19-1753-2022>, 2022.
- 20 Tai, A. P. K., Sadiq, M., Pang, J. Y. S., Yung, D. H. Y., and Feng, Z.: Impacts of Surface Ozone Pollution on Global Crop Yields: Comparing Different Ozone Exposure Metrics and Incorporating Co-effects of CO₂, *Front. Sustain. Food Syst.*, 5, 534616, <https://doi.org/10.3389/fsufs.2021.534616>, 2021.
- 25 Ueyama, M., Ichii, K., Kobayashi, H., Kumagai, T., Beringer, J., Merbold, L., Euskirchen, E. S., Hirano, T., Marchesini, L. B., Baldocchi, D., Saitoh, T. M., Mizoguchi, Y., Ono, K., Kim, J., Varlagin, A., Kang, M., Shimizu, T., Kosugi, Y., Bret-Harte, M. S., Machimura, T., Matsuura, Y., Ohta, T., Takagi, K., Takanashi, S., and Yasuda, Y.: Inferring CO₂ fertilization effect based on global monitoring land-atmosphere exchange with a theoretical model, *Environ. Res. Lett.*, 15, 084009, <https://doi.org/10.1088/1748-9326/ab79e5>, 2020.
- Val Martin, M., Heald, C. L., and Arnold, S. R.: Coupling dry deposition to vegetation phenology in the Community Earth System Model: Implications for the simulation of surface O₃, *Geophys. Res. Lett.*, 41, 2988–2996, <https://doi.org/10.1002/2014GL059651>, 2014.
- 30 Van Dingenen, R., Dentener, F. J., Raes, F., Krol, M. C., Emberson, L., and Cofala, J.: The global impact of ozone on agricultural crop yields under current and future air quality legislation, *Atmos. Environ.*, 43, 604–618, <https://doi.org/10.1016/j.atmosenv.2008.10.033>, 2009.
- Verbeke, T., Lathière, J., Szopa, S., and de Noblet-Ducoudré, N.: Impact of future land-cover changes on HNO₃ and O₃ surface dry deposition, *Atmospheric Chem. Phys.*, 15, 13555–13568, <https://doi.org/10.5194/acp-15-13555-2015>, 2015.
- 35 Verhoef, A. and Egea, G.: Modeling plant transpiration under limited soil water: Comparison of different plant and soil hydraulic parameterizations and preliminary implications for their use in land surface models, *Agric. For. Meteorol.*, 191, 22–32, <https://doi.org/10.1016/j.agrformet.2014.02.009>, 2014.



- Wang, Y., Jacob, D. J., and Logan, J. A.: Global simulation of tropospheric O₃-NO_x-hydrocarbon chemistry: 3. Origin of tropospheric ozone and effects of nonmethane hydrocarbons, *J. Geophys. Res. Atmospheres*, 103, 10757–10767, <https://doi.org/10.1029/98JD00156>, 1998.
- 5 Welp, L. R., Keeling, R. F., Meijer, H. A. J., Bollenbacher, A. F., Piper, S. C., Yoshimura, K., Francey, R. J., Allison, C. E., and Wahlen, M.: Interannual variability in the oxygen isotopes of atmospheric CO₂ driven by El Niño, *Nature*, 477, 579–582, <https://doi.org/10.1038/nature10421>, 2011.
- Wesely, M. L.: Parameterization of surface resistances to gaseous dry deposition in regional-scale numerical models, *Atmos. Environ.*, 23, 1293–1304, 1989.
- 10 Wild, B., Teubner, I., Moesinger, L., Zotta, R.-M., Forkel, M., van der Schalie, R., Sitch, S., and Dorigo, W. A.: VODCA2GPP – A new global, long-term (1988–2020) GPP dataset from microwave remote sensing, *Biosphere – Biogeosciences*, <https://doi.org/10.5194/essd-2021-209>, 2021.
- Wild, O.: Modelling the global tropospheric ozone budget: Exploring the variability in current models, *Atmos Chem Phys*, 7, 2643–2660, <https://doi.org/10.5194/acp-7-2643-2007>, 2007.
- 15 Wolf, S., Keenan, T. F., Fisher, J. B., Baldocchi, D. D., Desai, A. R., Richardson, A. D., Scott, R. L., Law, B. E., Litvak, M. E., Brunsell, N. A., Peters, W., and van der Laan-Luijkx, I. T.: Warm spring reduced carbon cycle impact of the 2012 US summer drought, *Proc. Natl. Acad. Sci.*, 113, 5880–5885, <https://doi.org/10.1073/pnas.1519620113>, 2016.
- Wong, A. Y. H., Geddes, J. A., Tai, A. P. K., and Silva, S. J.: Importance of dry deposition parameterization choice in global simulations of surface ozone, *Atmospheric Chem. Phys.*, 19, 14365–14385, <https://doi.org/10.5194/acp-19-14365-2019>, 2019.
- 20 Xia, L., Lam, S. K., Kiese, R., Chen, D., Luo, Y., van Groenigen, K. J., Ainsworth, E. A., Chen, J., Liu, S., Ma, L., Zhu, Y., and Butterbach-Bahl, K.: Elevated CO₂ negates O₃ impacts on terrestrial carbon and nitrogen cycles, *One Earth*, 4, 1752–1763, <https://doi.org/10.1016/j.oneear.2021.11.009>, 2021.
- Xu, B., Arain, M. A., Black, T. A., Law, B. E., Pastorello, G. Z., and Chu, H.: Seasonal variability of forest sensitivity to heat and drought stresses: A synthesis based on carbon fluxes from North American forest ecosystems, *Glob. Change Biol.*, 26, 901–918, <https://doi.org/10.1111/gcb.14843>, 2020.
- 25 Yan, M., Yue, X., Zhou, B., Sun, X., and Xin, N.: Projected changes of ecosystem productivity and their responses to extreme heat events in northern asia, *Front. Earth Sci.*, 10, 970296, <https://doi.org/10.3389/feart.2022.970296>, 2022.
- Yang, R., Wang, J., Zeng, N., Sitch, S., Tang, W., McGrath, M. J., Cai, Q., Liu, D., Lombardozi, D., Tian, H., Jain, A. K., and Han, P.: Divergent historical GPP trends among state-of-the-art multi-model simulations and satellite-based products, *Earth Syst. Dyn.*, 13, 833–849, <https://doi.org/10.5194/esd-13-833-2022>, 2022.
- 30 Yi, K., Dragoni, D., Phillips, R. P., Roman, D. T., and Novick, K. A.: Dynamics of stem water uptake among isohydric and anisohydric species experiencing a severe drought, *Tree Physiol.*, [treephys:tpw126v1](https://doi.org/10.1093/treephys/tpw126), <https://doi.org/10.1093/treephys/tpw126>, 2017.
- Yuan, H., Dai, Y., Xiao, Z., Ji, D., and Shanguan, W.: Reprocessing the MODIS Leaf Area Index products for land surface and climate modelling, *Remote Sens. Environ.*, 115, 1171–1187, <https://doi.org/10.1016/j.rse.2011.01.001>, 2011.
- 35 Yue, X. and Unger, N.: Ozone vegetation damage effects on gross primary productivity in the United States, *Atmospheric Chem. Phys.*, 14, 9137–9153, <https://doi.org/10.5194/acp-14-9137-2014>, 2014.



- Yue, X. and Unger, N.: The Yale Interactive terrestrial Biosphere model version 1.0: description, evaluation and implementation into NASA GISS ModelE2, *Geosci. Model Dev.*, 8, 2399–2417, <https://doi.org/10.5194/gmd-8-2399-2015>, 2015.
- 5 Yue, X., Unger, N., Harper, K., Xia, X., Liao, H., Zhu, T., Xiao, J., Feng, Z., and Li, J.: Ozone and haze pollution weakens net primary productivity in China, *Atmospheric Chem. Phys.*, 17, 6073–6089, <https://doi.org/10.5194/acp-17-6073-2017>, 2017.
- Zeng, X., Zhao, M., and Dickinson, R. E.: Intercomparison of Bulk Aerodynamic Algorithms for the Computation of Sea Surface Fluxes Using TOGA COARE and TAO Data, *J. Clim.*, 11, 2628–2644, [https://doi.org/10.1175/1520-0442\(1998\)011<2628:IOBAAF>2.0.CO;2](https://doi.org/10.1175/1520-0442(1998)011<2628:IOBAAF>2.0.CO;2), 1998.
- 10 Zeng, X., Shaikh, M., Dai, Y., Dickinson, R. E., and Myneni, R.: Coupling of the Common Land Model to the NCAR Community Climate Model, *J. Clim.*, 15, 23, 2002.
- Zhang, L., Moran, M. D., Makar, P. A., Brook, J. R., and Gong, S.: Modelling gaseous dry deposition in AURAMS: a unified regional air-quality modelling system, *Atmos. Environ.*, 36, 537–560, [https://doi.org/10.1016/S1352-2310\(01\)00447-2](https://doi.org/10.1016/S1352-2310(01)00447-2), 2002.
- Zhang, L., Brook, J. R., and Vet, R.: A revised parameterization for gaseous dry deposition in air-quality models, *Atmos Chem Phys*, 16, 2003.
- 15 Zhang, L., Jacob, D. J., Liu, X., Logan, J. A., Chance, K., Eldering, A., and Bojkov, B. R.: Intercomparison methods for satellite measurements of atmospheric composition: application to tropospheric ozone from TES and OMI, *Atmos Chem Phys*, 15, 2010.
- Zhang, L., Hoshika, Y., Carrari, E., Burkey, K. O., and Paoletti, E.: Protecting the photosynthetic performance of snap bean under free air ozone exposure, *J. Environ. Sci.*, 66, 31–40, <https://doi.org/10.1016/j.jes.2017.05.009>, 2018.
- 20 Zhang, Y. and Wang, Y.: Climate-driven ground-level ozone extreme in the fall over the Southeast United States, *Proc. Natl. Acad. Sci.*, 113, 10025–10030, <https://doi.org/10.1073/pnas.1602563113>, 2016.
- Zhang, Y. and Ye, A.: Improving global gross primary productivity estimation by fusing multi-source data products, *Heliyon*, 8, e09153, <https://doi.org/10.1016/j.heliyon.2022.e09153>, 2022.
- 25 Zhang, Y., Xiao, X., Wu, X., Zhou, S., Zhang, G., Qin, Y., and Dong, J.: A global moderate resolution dataset of gross primary production of vegetation for 2000–2016, *Sci. Data*, 4, 170165, <https://doi.org/10.1038/sdata.2017.165>, 2017.
- Zhao, Y., Zhang, L., Tai, A. P. K., Chen, Y., and Pan, Y.: Responses of surface ozone air quality to anthropogenic nitrogen deposition in the Northern Hemisphere, *Atmospheric Chem. Phys.*, 17, 9781–9796, <https://doi.org/10.5194/acp-17-9781-2017>, 2017.
- 30 Zhou, S. S., Tai, A. P. K., Sun, S., Sadiq, M., Heald, C. L., and Geddes, J. A.: Coupling between surface ozone and leaf area index in a chemical transport model: Strength of feedback and implications for ozone air quality and vegetation health, *Atmospheric Chem. Phys. Discuss.*, 1–23, <https://doi.org/10.5194/acp-2018-351>, 2018.
- Zhu, J., Tai, A. P. K., and Hung Lam Yim, S.: Effects of ozone–vegetation interactions on meteorology and air quality in China using a two-way coupled land–atmosphere model, *Atmospheric Chem. Phys.*, 22, 765–782, <https://doi.org/10.5194/acp-22-765-2022>, 2022.
- 35 Zielis, S., Etzold, S., Zweifel, R., Eugster, W., Haeni, M., and Buchmann, N.: NEP of a Swiss subalpine forest is significantly driven not only by current but also by previous year’s weather, *Discuss. Pap.*, 9, 2014.